



Assessing the contribution of understory sun-induced chlorophyll fluorescence through 3-D radiative transfer modelling and field data

Hornero^{a,c*}, A., North^a, P.R.J., Zarco-Tejada^{b,c}, P.J., Rascher^d, U., Martín^e, M.P.,
Migliavacca^f, M., Hernández-Clemente^a, R.

^a Department of Geography, Swansea University, SA2 8PP Swansea, United Kingdom

^b School of Agriculture and Food, Faculty of Veterinary and Agricultural Sciences and
Department of Infrastructure Engineering, Melbourne School of Engineering, University of
Melbourne, Melbourne, Victoria, Australia

^c Instituto de Agricultura Sostenible (IAS), Consejo Superior de Investigaciones Científicas
(CSIC), Alameda del Obispo s/n, 14004 Córdoba, Spain

^d Institute of Bio- and Geosciences, IBG-2: Plant Sciences, Forschungszentrum Jülich, Leo-
Brandt-Str, 52425 Jülich, Germany

^e Environmental Remote Sensing and Spectroscopy Laboratory (SpecLab), Spanish National
Research Council (CSIC), Albasanz 26-28, 28037 Madrid, Spain

^f Max Planck Institute for Biogeochemistry, Hans Knöll Straße 10, D-07745 Jena, Germany

**Corresponding author*

Submitted to Remote Sensing of Environment

April 2020

Revised September 2020

Abstract

A major international effort has been made to monitor sun-induced chlorophyll fluorescence (SIF) from space as a proxy for the photosynthetic activity of terrestrial vegetation. However, the effect of spatial heterogeneity on the SIF retrievals from canopy radiance derived from images with medium and low spatial resolution remains uncharacterised. In images from forest and agricultural landscapes, the background comprises a mixture of soil and understory and can generate confounding effects that limit the interpretation of the SIF at the canopy level. This paper aims to improve the understanding of SIF from coarse spatial resolutions in heterogeneous canopies by considering the separated contribution of tree crowns, understory and background components, using a modified version of the FluorFLIGHT radiative transfer model (RTM). The new model is compared with others through the RAMI model intercomparison framework and is validated with airborne data. The airborne campaign includes high-resolution data collected over a tree-grass ecosystem with the HyPlant imaging spectrometer within the FLuorescence EXplorer (FLEX) preparatory missions. Field data measurements were collected from plots with a varying fraction of tree and understory vegetation cover. The relationship between airborne SIF calculated from pure tree crowns and aggregated pixels shows the effect of the understory at different resolutions. For a pixel size smaller than the mean crown size, the impact of the background was low ($R^2 > 0.99$; NRMSE < 0.01). By contrast, for a pixel size larger than the crown size, the goodness of fit decreased ($R^2 < 0.6$; NRMSE > 0.2). This study demonstrates that using a 3D RTM model improves the calculation of SIF significantly ($R^2 = 0.83$, RMSE = $0.03 \text{ mW m}^{-2} \text{ sr}^{-1} \text{ nm}^{-1}$) when the specific contribution of the soil and understory layers are accounted for, in comparison with the SIF calculated from mixed pixels that considers only one layer as background ($R^2 = 0.4$, RMSE = $0.28 \text{ mW m}^{-2} \text{ sr}^{-1} \text{ nm}^{-1}$). These results demonstrate the need to

account for the contribution of SIF emitted by the understory in the quantification of SIF within tree crowns and within the canopy from aggregated pixels in heterogeneous forest canopies.

Keywords: chlorophyll fluorescence, heterogeneous canopies, hyperspectral, HyPlant, radiative transfer modelling, SIF, understory.

1. Introduction

International efforts have been carried out to monitor fluorescence from space in global studies using different sensors (Köhler *et al.*, 2018; Mohammed *et al.*, 2019) and modelling approaches (Verrelst *et al.*, 2015). One of the main challenges of the global low-resolution (over 60 m/pixel) sun-induced fluorescence (SIF) maps resides in the impact of the background components when quantifying SIF from large pixels aggregating different scene components. The first SIF global maps (Frankenberg *et al.*, 2011; Joiner *et al.*, 2011) were derived from the thermal and near-infrared sensor for observation (TANSO) onboard the greenhouse gases observing satellite (GOSAT) (Guanter *et al.*, 2012). A recent study has focused on downscaling SIF using the Global Ozone Monitoring Instrument 2 (GOME-2) and producing a daily corrected SIF global dataset with a spatial resolution of 0.05° (Duveiller *et al.*, 2020). The most recent SIF products based on the Orbiting Observatory 2 (OCO-2) launched in 2014 and the TROPOspheric Monitoring Instrument (TROPOMI) in 2018 provide a footprint of 1.3×2.25 km and 3.5×7 km at nadir respectively. OCO-2 and TROPOMI SIF products have the potential to provide GPP estimations for homogeneous vegetation type covers (Köhler *et al.*, 2018; Li *et al.*, 2018). Although these global maps were important achievements, questions were raised regarding the interpretation of

the SIF quantified from mixed pixels that aggregate vegetation, soil and shadow components (Xinchen Lu *et al.*, 2018). In the coming years, new possibilities of improving the spatial resolution of SIF global maps open up with the upcoming launch of the ESA Fluorescence Explorer (FLEX) satellite in 2022, designed to measure the instantaneous chlorophyll fluorescence signal with a very high spectral-resolution (0.1 nm) imaging spectrometer and a spatial resolution of 300 m. This will provide a completely new opportunity to assess the dynamics of actual photosynthesis through SIF, which offers a major advance over current capabilities that can only detect potential photosynthesis as derived through passive reflectance monitored by conventional Earth-resources satellites. The spatial resolution of FLEX is not, however, sufficient to understand the confounding effects of background components that affect the quantification of vegetation SIF at the pixel level. Recent initiatives, such as the FlexSense campaign (Siegmann *et al.*, 2019) for collecting airborne measurements at very fine resolution during the FLEX-Sentinel Tandem experiment, will contribute to the understanding and interpretation of SIF from aggregated pixels. Previous studies have attempted to interpret the SIF signal quantified at different scales, which is an important issue due to the effects of fractional vegetation cover and structure, and background (Zarco-Tejada *et al.*, 2013).

In heterogeneous forest and agricultural canopies, high-resolution images are required to enable the crowns and understory to be delineated from the background (Wagner *et al.*, 2018). The quantification of the contribution of each pixel helps to understand and to improve the models used to quantify biophysical parameters from mixed pixels (Yu *et al.*, 2018). The estimation of some of these parameters, such as the fraction of green vegetation (FC), leaf area index (LAI), or the fraction of absorbed photosynthetically active radiation (fAPAR), have critical implications in the estimation of Gross Primary Productivity (GPP) at the regional or global scale (Lin *et al.*,

2018; Tagliabue *et al.*, 2019). In fact, the impact of the understory on canopy reflectance is particularly challenging for studying complex canopies comprising different plant architectures and physiology (Eriksson *et al.*, 2006). Recent studies have demonstrated that SIF-GPP relationships not only are significantly affected by vegetation type (Li *et al.*, 2018; Sun *et al.*, 2018) but even vary within the same kind of vegetation (Migliavacca *et al.*, 2017). These studies concluded that finer resolution SIF observations were required to improve the accuracy of the models. However, it remains unclear how the covariation between SIF and GPP is affected by mixed vegetation from landscape to global scales (Sun *et al.*, 2017), although it has been shown that the canopy structure plays a dominant role in the SIF-GPP relationship (Dechant *et al.*, 2020; Duveiller *et al.*, 2020). Therefore, it is critical to quantify the contribution of each sub-pixel scene component in mixed canopies that are characterised by a heterogeneous distribution of trees and understory when working with satellite images at medium and low spatial resolutions.

Furthermore, temporal changes in the physiological condition and composition of the understory also affect the relationships between satellite data and vegetation properties, due to mixed pixel effects. This is especially the case at medium and low spatial resolutions, which alter temporal relationships, as demonstrated by Hornero *et al.* (2020). In that study, Sentinel-2 data was used to show an inverse relationship between vegetation indices and the increase in the disease incidence quantified from trees affected by *Xylella fastidiosa* (Xf) infection due to understory effects. The results demonstrated that the decrease in tree density, caused by the disease, produced an increase in the understory fraction, resulting in a controversial increase in the Normalized Difference Vegetation Index (NDVI) in the affected fields.

In this context, models are essential to relate observed optical properties to leaf biophysical and biochemical attributes and to analyse the effect of heterogeneous canopy structures at different

spatial resolutions (Wu and Li, 2009). Several methods have been proposed to calculate biochemical traits from hyperspectral reflectance, including scaling-up and model inversion methods that couple leaf and canopy transfer models (Verrelst *et al.*, 2018). For instance, recent studies (Melendo-Vega *et al.*, 2018) have used a coupled model strategy (1D PROSAIL + 3D FLIGHT) including the contribution of the grass background to improve the simulation of the spectral properties for multi-layered tree-grass ecosystems. Other strategies include the use of linear spectral unmixing techniques tested to separate the spectral properties of forest floor and overstory components (Markiet and Möttus, 2020). Despite the progress achieved, this modelling approach does not yet include the contribution of fluorescence and the impact of the multiple scattering produced between tree and understory components and the background layer.

In recent modelling studies, the chlorophyll fluorescence emission has been included at the leaf (Kallel, 2020; Pedrós *et al.*, 2010; Vilfan *et al.*, 2018, 2016) and canopy level in homogeneous (Atherton *et al.*, 2019; Romero *et al.*, 2020; Yang and van der Tol, 2018; Zeng *et al.*, 2019) and heterogeneous forest canopies (Hernández-Clemente *et al.*, 2017; Liu *et al.*, 2019; Zhao *et al.*, 2016). Furthermore, previous studies have attempted to account for spatial heterogeneity using the first available model-based approximations (Zarco-Tejada *et al.*, 2013). A more complex three-dimensional canopy radiative transfer model (RTM) – FluorFLIGHT (Hernández-Clemente *et al.*, 2017) – was developed to parameterise the canopy structure to estimate SIF from heterogeneous forest canopies. The model is based on the combination of FLUSPECT (Vilfan *et al.*, 2016) with the 3D ray-tracing model FLIGHT (North, 1996) to simulate multiple scattering within the canopy including the contribution of the gap and shadows between the tree crowns. Modelling results with FluorFLIGHT showed that the variability in the percentage of sunlit and

shaded vegetation and soil affects the absolute values of total SIF from aggregated pixels and therefore, the interpretation of SIF from coarse resolution images.

Despite the extensive work conducted with FLIGHT (Bye *et al.*, 2017; Hernández-Clemente *et al.*, 2017; Montesano *et al.*, 2015; Zarco-Tejada *et al.*, 2019, 2018), strategies that simulate SIF in heterogeneous canopies and consider the effects of different background components, such as soil type or understory fraction, have been limited by difficulties in simulating complex canopy structures and vertical heterogeneity. To simulate SIF of complex multi-scale plant architectures, another 3D ray-tracing approach, the Discrete Anisotropic Radiative Transfer (DART) model (Gastellu-Etchegorry *et al.*, 1996), has been proposed. This model has been recently used with data collected from a hand-held spectroradiometer to demonstrate that SIF is greatly influenced by canopy structure and understory vegetation (Liu *et al.*, 2019). However, further research is still necessary to understand the impact of structural components on the retrieval of SIF from medium (10 – 60 m/pixel) to high (0.3 – 10 m/pixel) spatial resolution satellite images. Airborne sensors such as HyPlant, the first fluorescence sensor designed to support the FLEX mission and dedicated to validating the retrieval of SIF for a large canopy and different vegetation types (Rascher *et al.*, 2015), can provide valuable information with which to model and understand better the effect of SIF signals among mixed pixels.

The impact of background components on SIF might particularly affect seasonal analyses, where the temporal variation of the understory fraction is high. Forest canopies, in particular, exhibit a complex canopy structure and the distribution of the understory cover fraction mainly depends on topography, sunfleck positions, soil composition and illumination conditions (Tagliabue *et al.*, 2019). Consequently, assuming an invariant and homogeneous effect of the soil as background might increase the uncertainty of biophysical parameters retrieved from high- and medium-

resolution imagery (Hornero *et al.*, 2020; Meng *et al.*, 2018). These previous studies have demonstrated the need to develop new modelling approaches that consider the multiple scattering, mutual shading of the crowns, variation in the soil, and shading of the background in SIF retrieval. In this study, we propose a modification of the 3D RTM FluorFLIGHT model to simulate canopy reflectance and SIF in heterogeneous canopies, including the effects of different background components, such as the soil and the understory cover fraction. In particular, we aim to i) analyse the contribution of SIF emitted by the understory in aggregated pixels using high spectral and spatial resolution imagery collected from the airborne hyperspectral HyPlant system, ii) study the impact of the variation in the understory cover fraction on the total SIF calculated at different scales. We compare this modified model with others from the Radiation Transfer Model Intercomparison (RAMI-3) exercise under the RAMI On-line Model Checker framework (ROMC) (Widlowski *et al.*, 2008, 2007) and validate it with field and airborne data.

2. Material and methods

2.1. Study site and ground data collection

The study was carried out in a Mediterranean tree-grass ecosystem (locally known as *dehesa*) located in Majadas de Tiétar (western Spain, 39°56'20"N, 5°46'28"W) (Fig. 1). The *dehesa* is a unique and practically endemic agrosilvopastoral system of the Iberian Peninsula, formed mainly by holm and cork oaks, with a lower stratum of grasses and shrubs, and generally shows extensive livestock use. These two strata, trees and understory, mainly define the vegetation structure in the study area. The tree layer covers approximately 20% of the surface and is predominantly composed of holm oak (*Quercus ilex* L. subsp. *ballota*) (Bogdanovich *et al.*, submitted). The

understory grass layer is highly dynamic and is dominated by species of the three main functional plant forms of grasses, forbs and legumes (Migliavacca *et al.*, 2017).

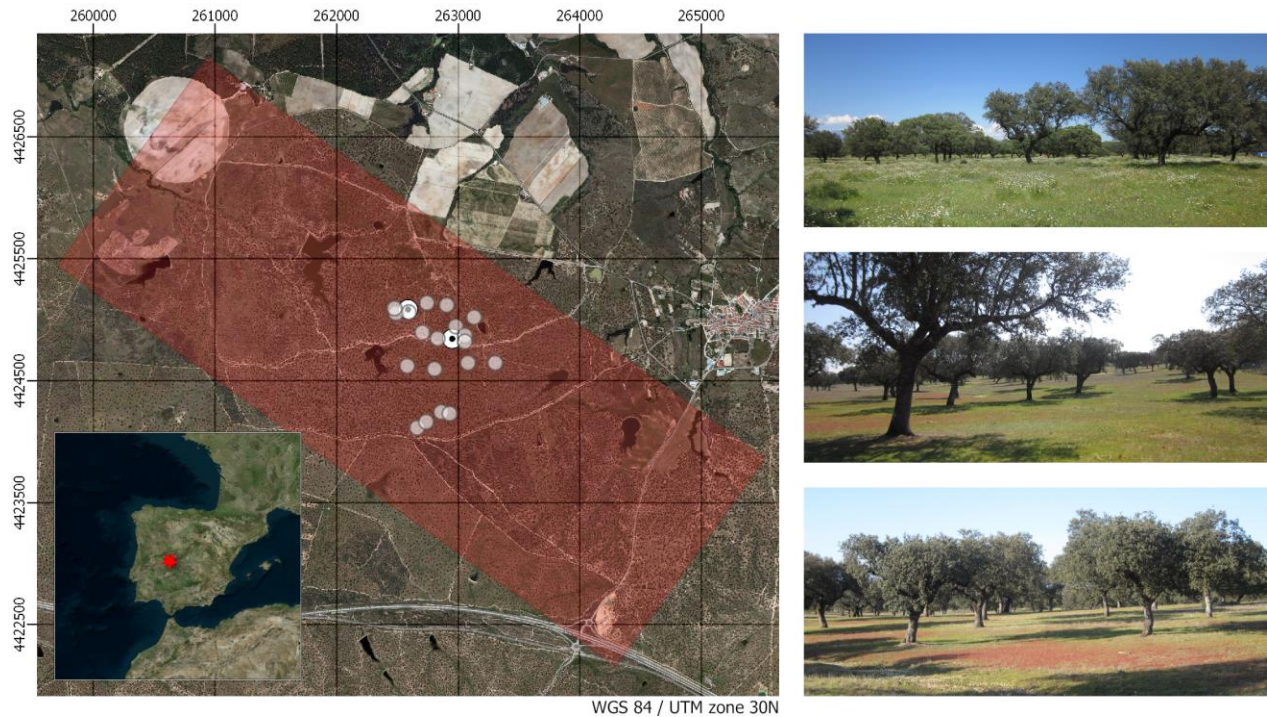


Figure 1. Location of the study site selected for the quantification of SIF through high-resolution hyperspectral imaging (left). The red shaded area represents the image coverage. The grey dots represent the 25×25 m plots that were sampled to obtain the biochemical and structural variables of the understory, and the white dotted circles represent the radiometric towers with FloX instruments attached measuring up- and down-welling radiance. The images on the right show the heterogeneity of the landscape and the understory within the area of study.

Field measurements were taken on 24 June 2018 simultaneously with the airborne campaign described in section 2.2 to perform the image processing and model parametrisation. In particular, total incoming radiance was required for the SIF and the reflectance calculation for both empirical and simulated data. Solar irradiance data were measured at the time of image acquisition with a SIF-enabled high-resolution spectroradiometer instrument (FloX, JB Hyperspectral Devices, Düsseldorf, Germany) mounted and levelled on a 9-metre tower above the tree canopy. Two FloX

boxes were installed over two trees (Fig. 1) during the flight, and another one was also used to collect spectral data from the understory in 15 plots (transects) between these trees. Each FloX equipment consists of two sealed and isolated spectroradiometers, FULL and FLUO (Table 1). Total incoming radiation was also simulated by the SMARTS model (National Renewable Energy Laboratory, United States Department of Energy) (Gueymard, 1995, 2001), using aerosol optical depth measured at 550 nm from the AERONET (Holben *et al.*, 1998) station over Majadas (Spain), located at a central point in the study area. A comparison between solar irradiance from different sources is presented in Fig. S1 (supplementary material).

Table 1

FloX specification. FULL and FLUO spectroradiometers used for the field data collection.

OPTIC	FULL	FLUO
Spectrometer-based model	FLAME VIS-NIR	QE Pro
Wavelength range (nm)	400 – 950	650 – 800
Spectral resolution (nm)	1.5	0.3
Signal-to-noise ratio	250	1000
Field of view (deg) (down- / up-welling radiance)	180 / 25	180 / 25

Biochemical and structural variables of the understory to enter into the model were obtained by destructive sampling of the grass layer in nineteen plots of 25×25 m located within the study area (Fig. 1). Two 25×25 cm grass samples were collected on each plot in areas visually identified to be representative of the variability in each plot; if the plot contained trees, one of the samples was acquired below the canopy to take into account the potential variability induced by the tree crowns (Melendo-Vega *et al.*, 2018; Mendiguren *et al.*, 2015). The understory leaf area index (LAI) was also measured by destructive sampling. All rooted plants within each 25×25

cm quadrant were collected using clippers and stored in sealed plastic bags. These were weighed in the field and then transported in a cooler to the laboratory, where subsamples were selected, and green and dry fractions were manually separated. Subsample fractions were scanned in an Epson Perfection V30 colour scanner (Epson American Inc., Long Beach, CA, USA). The leaf area was calculated automatically from the scanned images using the unsupervised classification algorithm ISOCLUS implemented in PCI Geomatica (PCI Geomatics, Richmond Hill, Ontario, Canada). ISOCLUS is based (with minor modifications) on the ISODATA method described in Tou *et al.* (1974). To measure the chlorophyll a (Ca), b (Cb), a+b (Cab) and total carotenoids (Cca) pigment concentration, a parallel grass sample (pigment quadrant) was taken adjacent to the quadrant where biophysical and structural variables previously described were sampled. In each pigment quadrant, the green fraction of the standing vegetation was sampled, weighed and frozen in dry ice in the field (for further details see Gonzalez-Cascon and Martin, 2018). The pigment concentrations in the homogenised grass sample were spectrophotometrically analysed in four replicates per sample using 80% (v/v) acetone as a solvent (Gonzalez-Cascon *et al.*, 2017). Percentage of dry mass was determined as well in three replicates per sample. All samples were then placed in an oven for 48h at a constant temperature of 60 °C to obtain their dry weight. Pigment concentrations per mass were determined in the green grass fraction material and calculated at 65 °C. Pigment content per total leaf area (µg/cm²) was calculated combining pigment concentrations per mass determined from the pigment quadrant and parameters obtained from the contiguous quadrant as:

$$C_{ab,leaf,grass} = \frac{1000 C_{ab,dmass,g} W_{d,s,v}}{A_{leaf,s}} \quad (1)$$

Where $C_{ab,dmass,g}$ (%) is the concentration of chlorophyll a + b per unit of dry mass of green grass measured in the pigment quadrant and $W_{d,s,v}$ (g) and $A_{leaf,s}$ (cm²) are the dry weight and leaf

surface area respectively of the green fraction of a subsample collected in the contiguous quadrant.

To characterise the tree canopy, leaf properties were measured for 19 individuals by destructive sampling using a Li-Cor 1800-12 integrating sphere (Li-Cor, Lincoln, NE, USA) coupled to an ASD Fieldspec 3 spectroradiometer (Analytical Spectral Devices Inc., Boulder, CO, USA). Leaves were obtained from two separate branches from the upper third of the tree crown on the south and north sides. The integrating sphere protocol is described by Zarco-Tejada *et al.* (2005), and further information regarding this sampling method is detailed in Melendo-Vega *et al.* (2018). Measurements of the tree canopy LAI were derived using an LAI-2200 plant canopy analyser (LI-COR, Lincoln, Nebraska, USA). Readings were taken above and below isolated trees under direct illumination conditions with the sensor facing $\pm 90^\circ$ to the solar azimuth angle. The FV2200 processing tool (LI-COR, Lincoln, Nebraska, USA), which provides a mechanism (Kobayashi *et al.*, 2013) that allows correction of measurements for radiation reflected and transmitted by the foliage, was used to apply scattering corrections and to calculate LAI using crown-shape measurements derived from field images.

2.2. Airborne hyperspectral and LiDAR data

Airborne data collection (Fig. 2) was conducted on 24 June 2018 using the high-resolution triple-coupled hyperspectral solution HyPlant v3, developed by the Jülich Research Centre (Kreis Dören, Germany) in cooperation with SPECIM Spectral Imaging Ltd. (Oulu, Finland) (Siegmann *et al.*, 2019) and a long-range laser scanner onboard a Cessna aircraft. The HyPlant system consists of two hyperspectral modules as a combination of three pushbroom imaging line

scanners. The DUAL imager (available commercially as AisaFENIX) comprises two integrated sensors in a single housing sharing the same optics, which provides continuous spectral information covering the visible/near-infrared (VNIR) and short-wave infrared (SWIR) regions of the spectrum (380 – 2500 nm), and yielding 3.5 and 12 nm full-width at half-maximum (FWHM) spectral resolution, respectively. The FLUO module (commercially known as AisaIBIS) is an imager that acquires data between 670 and 780 nm at higher spectral resolution (Celesti *et al.*, 2019; Siegmann *et al.*, 2019). The hyperspectral sensors were radiometrically calibrated with an integrating sphere on SPECIM's facilities by calculating coefficients derived from a calibrated light source and, prior to applying these coefficients, the dark frame correction was conducted. We calculated the top-of-canopy (TOC) spectral reflectance – Cluster II output as described in Siegmann *et al.*, (2019) – from the DUAL imager in the VNIR and SWIR regions with ATCOR4 (ReSe Applications Schläpfer, Wil, Switzerland) using available sunphotometer measurements of Aerosol Optical Depth (AOD) as input parameters. We used at-sensor-radiance from the FLUO imager (Cluster III output), extended by the application of the point-spread function deconvolution (Siegmann *et al.*, 2019). DUAL and FLUO sensors were boresight corrected and orthorectified with CaliGeoPRO (SPECIM Spectral Imaging Ltd., Oulu, Finland) using inputs from an inertial navigation system Oxford 3052 GPS/INS (Oxford Technical Solutions Ltd., Oxford, UK) installed on-board and synchronised with HyPlant.

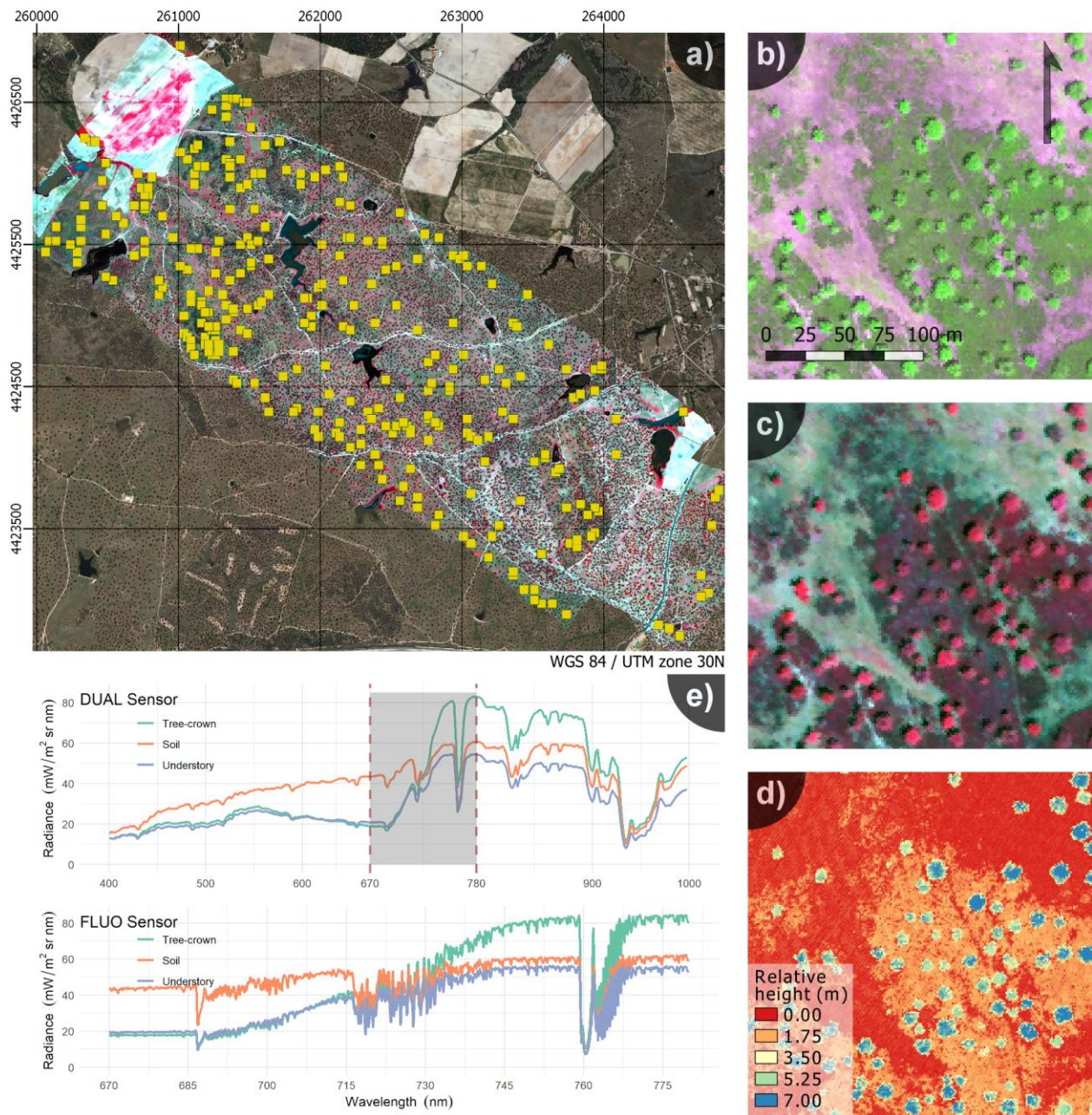


Figure 2. Airborne high-resolution hyperspectral flight with the HyPlant sensors (colour-infrared, {860, 650, 550 nm}) over the study area (a). Yellow squares indicate the location of the 300, 25 × 25 m, scene grid selection. The different components that comprise a scene can be visually discriminated by the images acquired from b) the FLUO (false colour, {700, 754, 674 nm}) and c) DUAL (colour-infrared) sensors of the HyPlant tandem and d) from the digital surface model of the LiDAR sensor. Spectral radiance extracted from tree crowns, understory (shrubs and grasses) and soil components of Hyplant DUAL+FLUO images is shown in (e).

LiDAR data were acquired using a Riegl LMS-Q780 system (RIEGL Laser Measurement Systems GmbH, Horn, Austria). A normalised digital surface model (nDSM), also known as canopy height model and generated from the LiDAR point cloud, was used to measure canopy features: height, diameter and fractional cover (FC). The nDSM product also allowed image segmentation to be performed, to separate tree crowns from the understory.

The hyperspectral images had a ground resolution of 1.5 metres per pixel and allowed individual tree crowns to be distinguished from the background consisting of soil and understory vegetation. We used the images to calculate the spectral information of each scene component (Fig. 3), to calculate the NDVI (Rouse *et al.*, 1974) and to quantify the fluorescence signal. For this, we used the O₂ A-band in-filling method through the Fraunhofer Line Depth (FLD) principle (Plascyk, 1975), based on a total of three spectral bands (3FLD) (Maier *et al.*, 2003);

$$3FLD = \frac{E_{out} \cdot L_{in} - E_{in} \cdot L_{out}}{E_{out} - E_{in}} \quad (2)$$

where radiance L corresponds to L_{in} (at 761 nm), L_{out} (mean value of L_{747} and L_{780} spectral bands), and irradiance E to E_{in} (at 761 nm), and E_{out} (mean value of E_{747} and E_{780} spectral bands). The decision of using 3FLD is based on the successful performance of this index in previous studies (Cendrero-Mateo *et al.*, 2016; Damm *et al.*, 2015; Liu *et al.*, 2015; Liu and Liu, 2014). 3FLD was calculated by using the at-sensor-radiance from the FLUO imager previously described, which does not take into account the atmospheric absorption and scattering effects. For this study, we assumed relatively low impact of these effects considering that we are assessing the relative contribution of SIF emitted by the understory to the full canopy with data collected from a single flight and acquired within 27 minutes in clear sky conditions. In addition, a comparison was made between FloX measurements and the hyperspectral images. Using all the measured data (transects

and tree-crown measurements) the relationship was reasonably strong ($R^2 = 0.67$, $\text{RMSE} = 0.12 \text{ mW m}^{-2} \text{ sr}^{-1} \text{ nm}^{-1}$), improving when the assessment was carried out using the two FloX instruments permanently installed over two tree crowns ($\text{RMSE} = 0.04 \text{ mW m}^{-2} \text{ sr}^{-1} \text{ nm}^{-1}$).

The objective of using NDVI in this study is to show the behaviour of a standard and widely used vegetation index related to fractional cover, comparing the effects observed in both NDVI and SIF. The high-spatial resolution of the airborne hyperspectral images allowed the extraction of different scene components used as ground truth used for the model inversion following the methodology proposed by Zarco-Tejada *et al.* (2019). A Mahalanobis Distance classification (Richards, 1999) using ENVI/IDL (Exelis Visual Information Solutions, Boulder, Colorado) was also derived from the hyperspectral DUAL-sensor imagery to classify vegetation cover, soil, roads and water ponds throughout the study area. In this way, we constructed the scene grid and filtered scenes that contained roads, water or buildings. The scene grid enabled the spectral reflectance of each component to be calculated, which was then used to evaluate the behaviour of the model with different types of soil, understory variability and FC (Fig. 2).

We used the tree-crown segmentation calculated from the nDSM LiDAR product to establish an external buffer of two metres, which was excluded from the analysis to avoid tree shadows, mixtures of tree branches and understory at the crown edges, and potential effects of misalignment between sensors (Fig. 3).

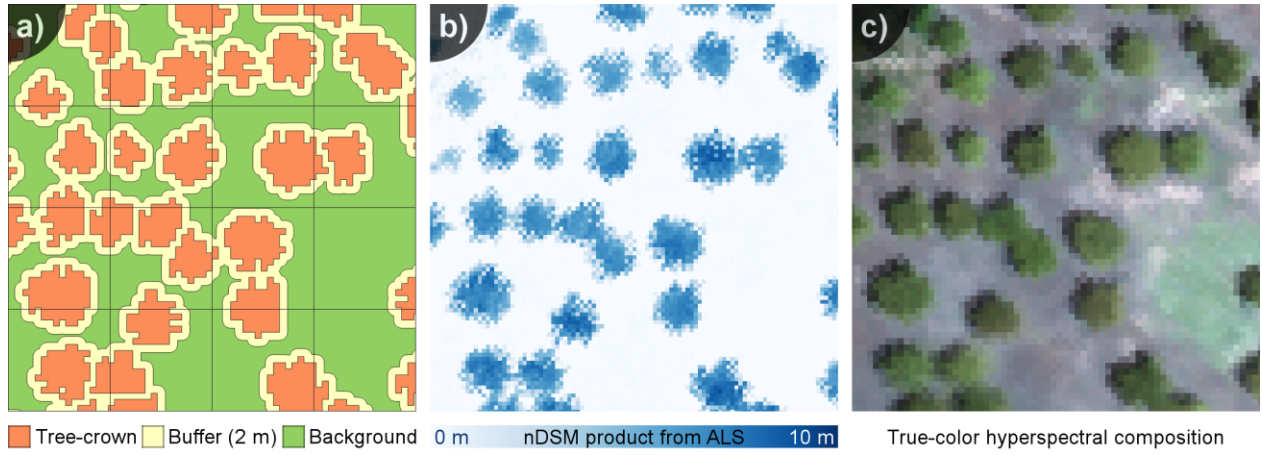


Figure 3. Example of a) tree-crown delineation over the b) normalised digital surface model (nDSM) and the c) True colour DUAL orthoimage.

Taking into account the difference in NDVI and 3FLD values obtained from tree-crown and aggregated pixels (Fig. 4), we performed an empirical analysis over a selection of 300 scenes (Fig. 2a) that covered all the natural range found within the study area (NDVI: 0.25 – 1.00, 3FLD: 0.10 – 0.95 $\text{mW m}^{-2} \text{sr}^{-1} \text{nm}^{-1}$).

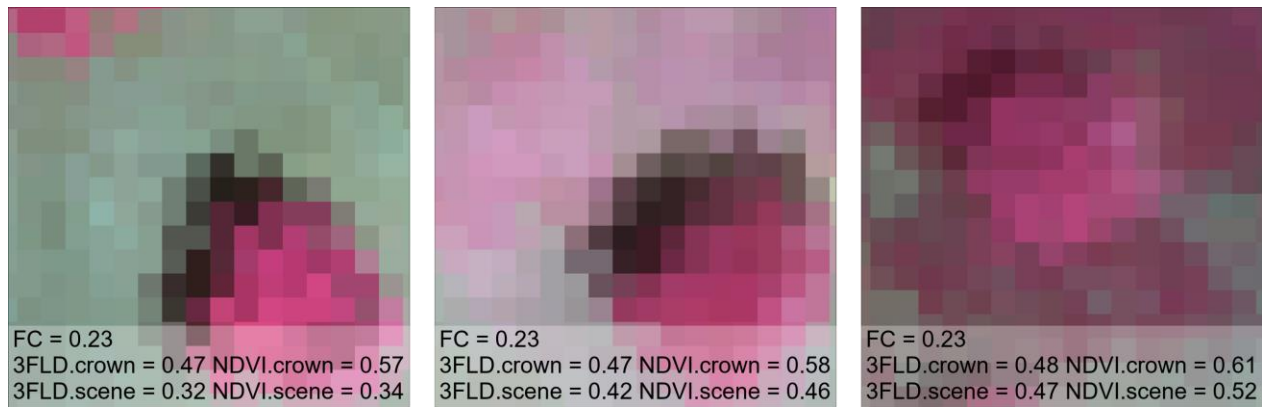


Figure 4. Understory variability in different scenarios (colour-infrared composition; 25×25 m pixels along with the collected data) and how this variation affects the mean value in the NDVI (unitless) and 3FLD ($\text{mW m}^{-2} \text{sr}^{-1} \text{nm}^{-1}$) indices.

354 To assess the contribution of SIF emitted by the understory, we compared the values obtained
355 from tree crowns and aggregated pixels at different spatial scales (Fig. 5a). We selected the spatial
356 resolutions of 5, 15, 25, 50 and 100 m (Fig. 5b), which were either smaller than the tree crowns
357 or much larger and even grouped several trees within the same sampling. Figures 5c and 5d show
358 that NDVI and 3FLD values of the scene decrease as pixel aggregation increases. The spatial
359 resolution selected is highlighted in different colours covering different aggregation levels
360 covering the entire range. Those resolutions were used to further analyse the contribution of the
361 SIF emitted by the understory and tree crowns using empirical data and RTM as described below.

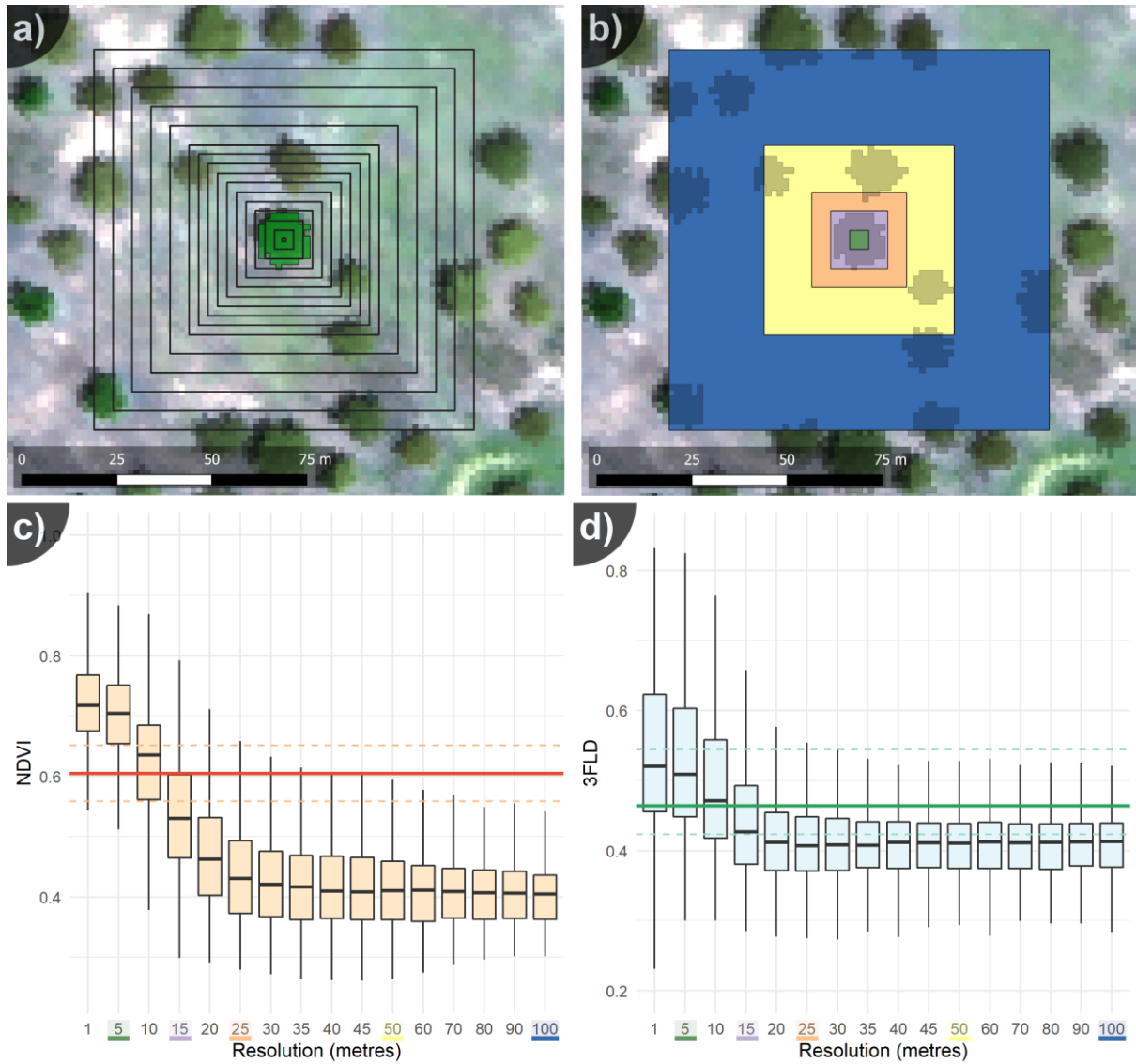


Figure 5. Spatial scales from 1 to 100 m (a) and its selection (b) at 5 m (green), 15 m (purple), 25 m (orange), 50 m (yellow) and 100 m (blue). Aggregated values of c) NDVI and d) 3FLD ($\text{mW m}^{-2} \text{sr}^{-1} \text{nm}^{-1}$) at different spatial scales from a); horizontal lines show the mean tree-crown value and the Q1-Q3 interquartile range.

2.3. Modified FluorFLIGHT Model to account for the understory

In this study, we extended the 3D RTM FLIGHT (North, 1996) to account for the understory layer, including the SIF contribution of the crowns from the FluorFLIGHT modification (Hernández-Clemente *et al.*, 2017). The main reason for using this model is that it has been

previously validated in several applications for the quantification of biophysical parameters (Bye *et al.*, 2017; Guillen-Climent *et al.*, 2012) and plant health condition (Hernandez-Clemente *et al.*, 2017; Hornero *et al.*, 2020; Zarco-Tejada *et al.*, 2018). Furthermore, the computational speed of FLIGHT is relatively fast if compared to other more complex 3D models (DART, Raytran or Librat) because sunlit and shaded canopy fractions are based on simple geometrical-optical properties as reviewed in Malenovsky *et al.* (2019). The model is available for download on <https://flight-rtm.github.io>.

The modification, named FLIGHT8, is based on the existing theory of RTM and couples an additional layer into the 3D ray-tracing model FLIGHT to account for the understory, including changes related to SIF and the interaction between the existing and new components (Fig. 6). We considered the contribution of SIF within the understory, as well as the multiple scattering events between components. Similar to FluorFLIGHT, this approach is also coupled with the leaf fluorescence model FLUSPECT (Vilfan *et al.*, 2016), which is a physical model based on Kubelka-Munk theory that includes the fluorescence quantum efficiency parameterisation according to its core-original model PROSPECT (Feret *et al.*, 2008; Jacquemoud and Baret, 1990).

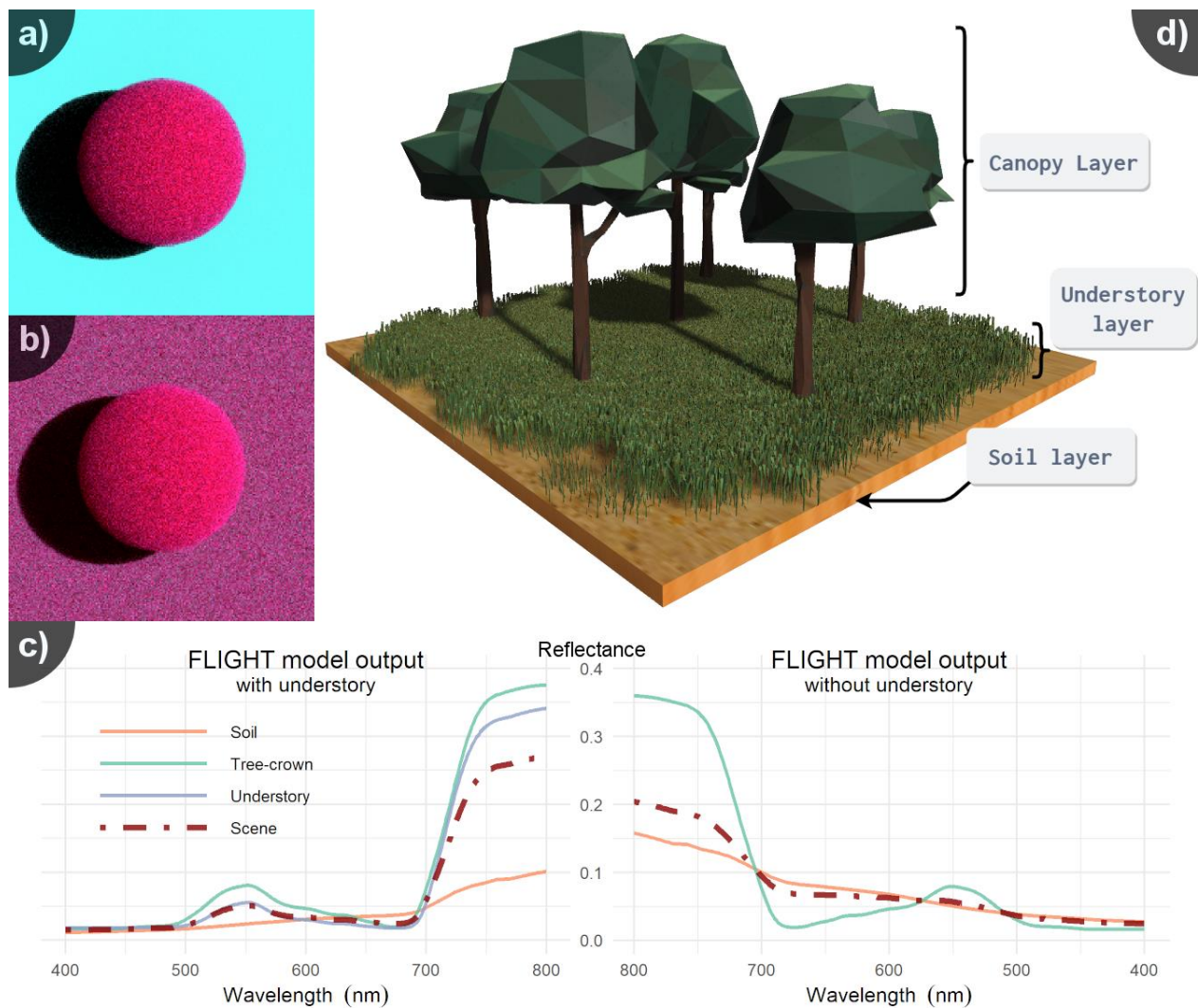


Figure 6. Example tree-canopy simulations a) without and b) with understory, c) including their spectra; d) graphical representation of FLIGHT8.

The Monte Carlo ray-tracing model FLIGHT was designed to rapidly simulate light interaction with 3D vegetation canopies at high-spectral resolution, to produce reflectance spectra and lidar returns for both forward simulation and use in inversion (North, 1996; North *et al.*, 2010), and recently extended to model solar-induced fluorescence (Hernández-Clemente *et al.*, 2017). Foliage is represented by structural properties of leaf area, leaf angle distribution, crown dimensions and fractional cover, and the optical properties of leaves, branch, shoot and ground

components. The model explicitly represents multiple scattering and absorption of light within the canopy and with the ground surface and used as a benchmark by the Radiative Transfer Model Intercomparison (RAMI) (Widlowski *et al.*, 2007). Scattering within crown and understory components is evaluated by the Monte Carlo method of radiative transfer modelling approximation, where a photon can be stochastically either absorbed or scattered into a new direction. Outside these components, the photon trajectory simulation proceeds by a deterministic ray-tracing approach.

The new model includes an additional parameterisation that defines the understory layer. The understory extends from the soil layer (Fig. 6d) to a user-defined height. More input values were added to also define the understory leaf size and its distribution (leaf angle distribution), as well as the mean one-sided total foliage area index (LAI). At leaf level, both the existing model and the understory addition use the same equations (3) to (6) described below to calculate radiance, with appropriate values for optical and structural properties, and here detailed for understory.

Within the homogeneous understory layer, the illumination of a leaf is calculated as the sum of direct and diffuse incoming light. For a leaf L_{US} , viewed from direction vector Ω and illuminated from vector Ω_0 , the contribution of the radiation leaving the surface to the detector without taking into account the fluorescence is defined as follows:

$$I_{L_{US}}(\lambda) = I_0(\lambda)\gamma_{L_{US}}(\lambda, \Omega_0 \rightarrow \Omega)P_0 + \frac{1}{m}\sum_1^m I_m(\lambda, \Omega_m) \gamma_{F_{US}}(\lambda, \Omega_m \rightarrow \Omega) \quad (3)$$

where I_0 corresponds to the illumination radiance of the direct solar beam at the wavelength λ , I_m represents the sample of the incoming diffuse field from the Ω_m direction, and $\gamma_{L_{US}}$ denotes the bidirectional reflectance/transmittance factor for each leaf from the understory. If there is a direct path to the light source, P_0 has a value 1, and 0 if not. The incoming diffuse light field is sampled

using m directions over a sphere. Each sample traces a ray from the leaf to the next interaction in that direction, or sky, and which may leave the understory canopy and so be a contribution from non-understory components; radiance from this is calculated recursively using (3). The non-fluorescent scattering phase function within the understory component at wavelength λ and leaf normal vector Ω_L , has been approximated using a bi-Lambertian reflectance model:

$$\gamma_{LUS}(\lambda, \Omega_L, \Omega' \rightarrow \Omega) = \begin{cases} \pi^{-1} \rho_n(\lambda) |\Omega \cdot \Omega_L|, & (\Omega \cdot \Omega_L)(\Omega' \cdot \Omega_L) < 0 \\ \pi^{-1} \tau_n(\lambda) |\Omega \cdot \Omega_L|, & (\Omega \cdot \Omega_L)(\Omega' \cdot \Omega_L) > 0 \end{cases} \quad (4)$$

Following similar equations, the fluorescence contribution for an individual leaf within this layer (F_{LUS}) is calculated using full fluorescent scattering matrices, through sampling direct and diffuse incident illumination within the excitation range from 400 to 750 nm:

$$F_{LUS}(\lambda) = \sum_{k=400}^{750} \left(I_0(k) \gamma_{FUS}(k, \lambda, \Omega_0 \rightarrow \Omega) P_0 + \frac{1}{m} \sum_{1}^m I_m(k, \Omega_m) \gamma_{FUS}(k, \lambda, \Omega_m \rightarrow \Omega) \right) \quad (5)$$

where γ_{FUS} :

$$\gamma_{FUS}(k, \lambda, \Omega_L, \Omega' \rightarrow \Omega) = \begin{cases} \pi^{-1} Mb[k, \lambda] |\Omega \cdot \Omega_L|, & (\Omega \cdot \Omega_L)(\Omega' \cdot \Omega_L) < 0 \\ \pi^{-1} Mf[k, \lambda] |\Omega \cdot \Omega_L|, & (\Omega \cdot \Omega_L)(\Omega' \cdot \Omega_L) > 0 \end{cases} \quad (6)$$

where Mb and Mf represent the backward- and forward-scattering fluorescence matrices for both photosystems PS-I and PS-II, respectively. Similar to FluorFLIGHT at tree-crown level, total measured radiance in the understory component is calculated as the sum of the reflected light (I_{LUS}) and fluorescent emission contribution (F_{LUS}).

The other components within the scene (Fig. 6d), the fluorescence contribution within a tree crown, and the consideration of the incident diffuse field remain as described in North (1996), North *et al.* (2010) and Hernández-Clemente *et al.* (2017). The Monte Carlo formulation allows the leaf-level fluorescence contribution to be readily scaled by an estimate of local fluorescence

quantum efficiency if available. While single constant values are used separately for understory and canopy here, other recent studies have explored separation of values for sunlit and shaded leaves, or parameterisation by leaf-level PAR (Gastellu-Etchegorry *et al.*, 2017; Zeng *et al.*, 2020; Zhao *et al.*, 2016).

To evaluate the included features in FLIGHT8, we compared the new understory layer as a single 1D simulation with homogeneous cases from the RAMI-3 experiments (Widlowski *et al.*, 2007), which is the most recent and updated RAMI phase built for this purpose. No crowns were considered in this comparison because there is no existing model intercomparison that accounts for a two-layer homogeneous (HOM) and heterogeneous (HET) approach; for fluorescence there is no agreed intercomparison to date. A more recent experiment, RAMI-IV, featured a completely new set of experiments for abstract canopies (Widlowski *et al.*, 2013), but this exercise neither included any case with the HOM-HET combination nor purely homogeneous scenes.

One of the difficulties in evaluating an RT model by comparison with other models is the absence of an absolute reference standard; therefore, to compare the output of the model with a reference value, an alternative truth should be identified. This truth was generated as the mean of a series of models that were identified during the third phase of the RAMI-3 exercise. The radiative transfer models DART (Gastellu-Etchegorry *et al.*, 1996), Drat (Lewis, 1999), FLIGHT (North, 1996), Rayspread (Widlowski *et al.*, 2006), Raytran (Govaerts and Verstraete, 1998) and Sprint (Thompson and Goel, 1998) participated in the generation of the reference data (RAMIREF).

To cover the entire range of the different inputs (Table S1, supplementary material), we summarised the intercomparison in 12 cases for the Bi-directional Reflectance Factor (BRF) in the principal planes and orthogonal planes by varying the solar viewing angles. Root Mean

Squared Error (RMSE) and Mean Absolute Error (MAE) were then calculated between the simulated signal and the RAMIREF.

2.4 Model simulation approaches

Firstly, we evaluated the SIF of the understory on a theoretical set of simulations with a single tree by varying its fluorescence quantum efficiency (F_i from 0 to 0.05) and setting the LAI to the maximum nominal value ($LAI = 3$). Under the tree canopy, we defined an understory layer and varied its F_i (from 0 to 0.05) and LAI (from 0 to 3). These analyses aimed to understand the contribution of the SIF emitted by the understory layer with a minimum impact from structural tree canopy variables and shadowing.

A more complex scenario was then designed to evaluate the impact on the SIF calculated by aggregating the tree canopy and the understory components. For this purpose, high-resolution airborne images were used to set up the different scenes, and field measurements were taken to establish ranges of biophysical parameters and biochemical variables (Table 2). The parameters required by the models that could not be measured in the field (leaf mesophyll structure, leaf angle distribution, senescence material and fluorescence quantum efficiency) were established through previous studies using the values evaluated by Hernandez-Clemente *et al.*, (2017) for oak trees and by Melendo-Vega *et al.* (2018) for the understory.

Table 2
Values used in the model simulation analysis.

Variable	Units	Acronym	Range
Chlorophyll a+b content	$\mu\text{g cm}^{-2}$	Cab	0 – 64
Carotenoid content	$\mu\text{g cm}^{-2}$	Cca	0 – 30

Water content	cm	Cw	0 – 0.03
Dry matter content	g cm ⁻²	Cdm	0.003 – 0.018
Senescence material	Fraction	Cs	0 – 0.3
Mesophyll structure	-	N	1 – 3
Fluorescence quantum efficiency	-	F _i	0 – 0.2
Leaf Area Index	m ² m ⁻²	LAI	0 – 3
Leaf Size	m	LFS	0.01 – 0.05
Leaf angle distribution	-	LAD	Spherical
Soil reflectance	ρ _{lsoil}	Soil	4 samples
Solar Zenith	deg.	SZA	25.84
Solar Azimuth	deg.	SAA	122.89

482

483 The inversion scheme was a multi-step LUT-based approach using NDVI, 3FLD and 650 – 800
484 nm as described in Hernández-Clemente *et al.* (2017). In the first stage of the analysis, we built
485 a lookup-table (LUT) of +400k simulations by coupling FLUSPECT-B with FLIGHT8 in 1D
486 mode. The LUT is used to estimate leaf parameters and LAI from the tree canopy and understory
487 independently. The inversion was carried out in different steps by minimising the merit function
488 consecutively for LAI and leaf biochemical parameters. In the next stage, the parameterisation
489 retrieved for each of the scenes and components was used in a second set of simulations by
490 coupling FLUSPECT-B with FLIGHT8 in 3D mode. The topography in the simulations was
491 simplified as flat terrain. The forward simulations were used to calculate the aggregated value of
492 NDVI and 3FLD for the 300 scenes of 25 m selected as described in section 2.2. This last step
493 was applied using FLIGHT8 in two different modes, accounting for the specific contribution of
494 SIF emitted by the understory layer (full mode) and disabling the SIF emitted by the understory

495 (single mode). Model simulations in single-mode use only one layer for the background (assumed
496 Lambertian) and, for this analysis, we used the mean spectral reflectance extracted from the image
497 which includes the average proportion of soil and understory found in the study area. Finally, the
498 model-simulated aggregated pixel, from both the full- and single-mode approaches, was
499 compared to that extracted from the hyperspectral image. The modelling approach performed is
500 depicted in Fig. 7. The comparison between single-mode and full-mode approach was intended
501 to understand the theoretical contribution of the understory integrated into FLIGHT8.

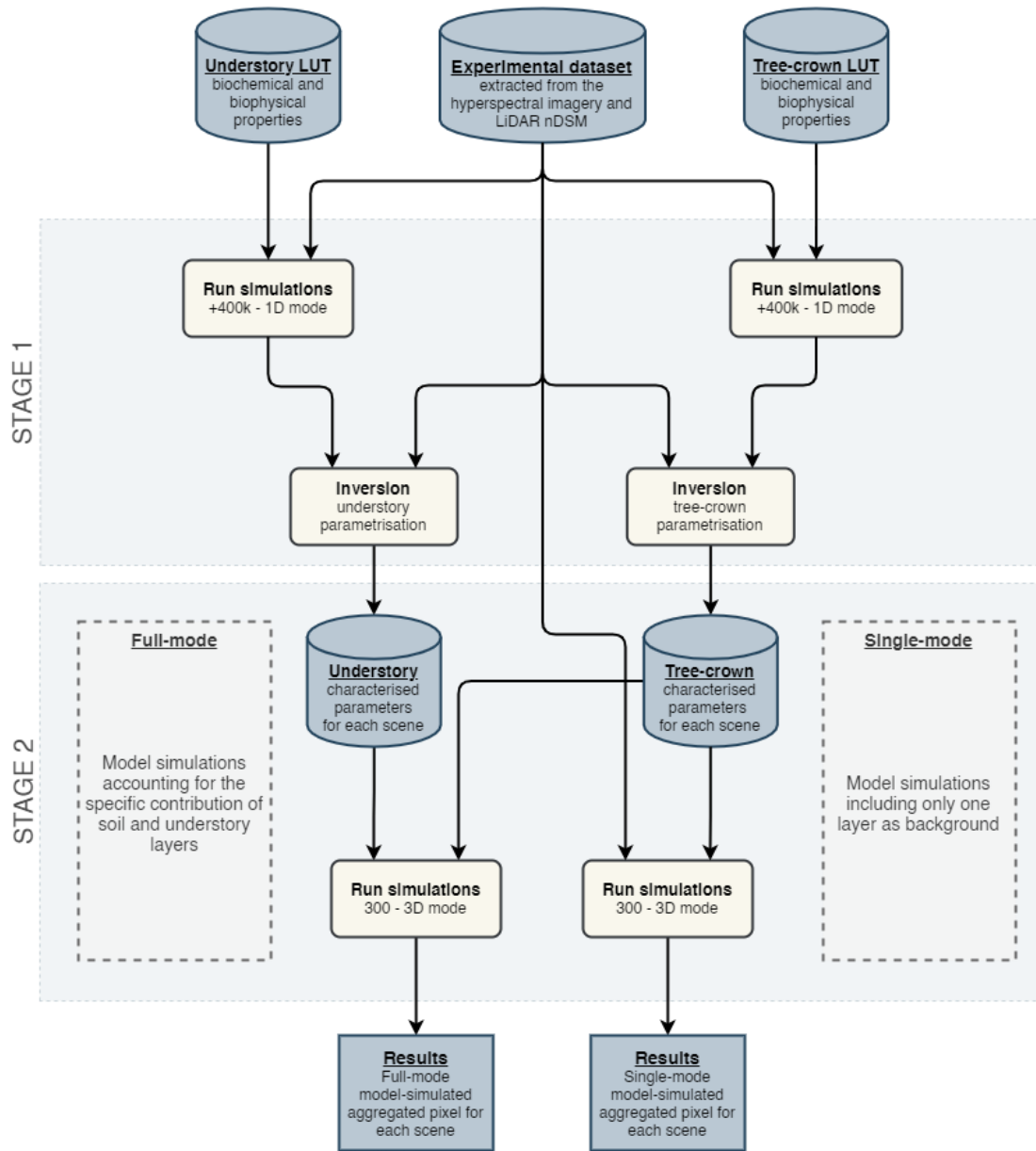


Figure 7. Model simulation approach diagram.

3. Results

Results from empirical approaches are presented to show the effect of the understory on NDVI and 3FLD derived from different pixel aggregation scales. Based on the need to correct these effects, we present results showing the performance of FLIGHT8 to account for the understory variations that affect the reflectance calculated from aggregated pixels. FLIGHT8 was additionally compared with other models and widely accepted reference data.

3.1. Effects of the understory on airborne data calculated from aggregated pixels

The comparison between the aggregated pixel and the tree-crown segmented value extracted from the airborne imagery showed the impact of the background at different scales for NDVI and 3FLD indices (Fig. 8a and 8b, respectively). In the case that the aggregated pixel includes more than one tree (Fig. 5), these are taken into account when computing the average value of the tree-crown and understory components. At a resolution of 5 m, where aggregated areas were centred on crowns (green points in Fig. 8a, b), the pixel size was smaller than the mean crown size ($\mu\phi = 11.98$ m), and the impact of the background was relatively low for both NDVI and 3FLD, with a high correlation between aggregated and pure crown values ($R^2 > 0.99$; NRMSE < 0.01). The goodness of fit between tree-crown and aggregated pixels decreased with a pixel size slightly higher than the crown size (15 m), and the errors doubled with a crown size of 25 m (orange points) for NDVI ($R^2 = 0.47$; NRMSE = 0.33) and 3FLD ($R^2 = 0.58$; NRMSE = 0.2). To elucidate the contribution of each component at this scale, we plotted the relationship between the canopy and the understory FC (Fig. S2, supplementary material). The dispersion of points increased and diverged from a linear fitting as the soil FC increased. The contribution of each component at the same resolution (25 m, Fig. 8c and 8d) showed that the slope of the linear relationship between

the NDVI from aggregated pixels and understory was closer to the identity line than that of the tree crowns, confirming that the contribution of the understory is significant.

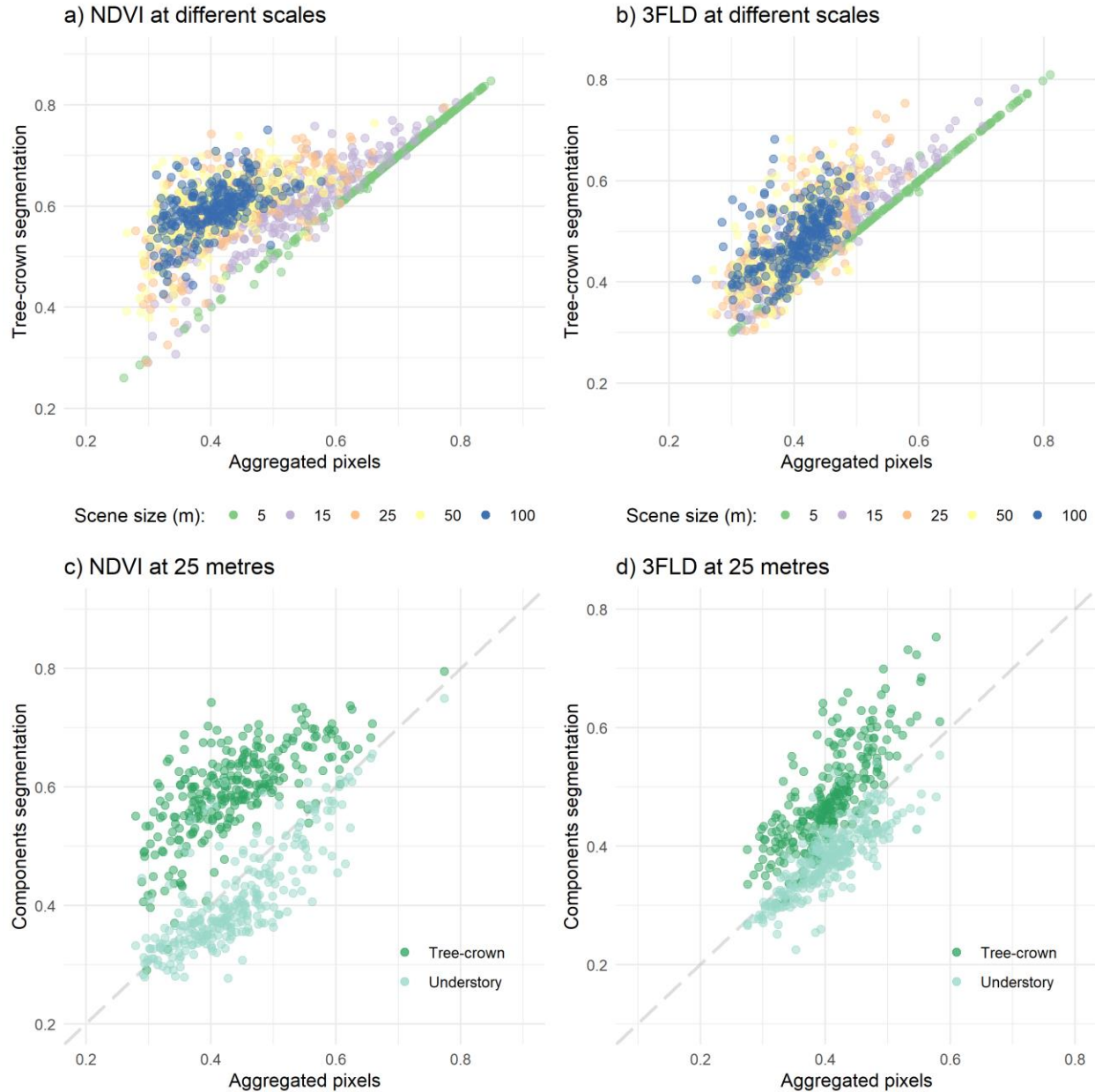


Figure 8. Relationship between airborne image data obtained from pure tree crowns and aggregated pixels from a 5 m window to a 100 m window for a) NDVI and b) 3FLD ($\text{mW m}^{-2} \text{sr}^{-1} \text{nm}^{-1}$). Spatial scales start at 5 m (green points) and increase to 15, 25, 50 and 100 m (purple, orange, yellow and blue points, respectively). Relationship between c) NDVI and d) 3FLD values aggregated by tree-crown and understory components, and the total aggregated value at 25 m.

3.2. The FLIGHT8 model approach to account for background effects

As a previous step to the modelling approach, the performance of FLIGHT8 was analysed using controlled conditions. A comparison against other RTM models is included in supplementary material. Fig. S3 shows that the simulations obtained (dark-green line) through the range of input variables agreed in RAMI showed a similar performance to that of the models used to generate the reference data RAMIREF (dashed light-green line). The shaded yellow area displays the absolute coverage range of these models, and in all cases, the simulations with FLIGHT8 were contained within this zone. More comparison results are presented in supplementary material (Fig. S4), including the results from the RAMI On-line Model Checker (ROMC). In all cases, the observed degree of relationship between the reference value and the simulations from the modified model was very high, showing a coefficient of determination (R^2) that exceeded 0.98, with a mean value of 0.99. The differences between these data sets were also minimal, and the greatest error was 0.007 for both RMSE and MAE metrics. The first set of results showed the sensitivity of aggregated pixel 3FLD to variation in the understory and tree-crown F_i and the understory LAI (Fig. 9). The total scene SIF increases with LAI and the F_i of both the understory and crowns (Fig. 9a). Understory LAI is shown to have the greatest impact on aggregate pixel SIF for the ranges shown. Within each subgroup of LAI (0.5 size step), there was a gradual increase in the variation in the aggregated pixel, which followed a similar pattern, except when the understory LAI was zero, where the scene SIF only varied depending on the tree parametrisation. For values of LAI in the understory above zero, a similar increase in SIF of the scene was observed with increasing values of understory and tree-crown F_i . Furthermore, there was a linear relationship between the SIF extracted from sunlit (Fig. 9b left) and full-crown pixels (Fig. 9b right) with respect to the aggregated pixels as a function of the variation in F_i (0 – 0.05)

of the understory and the tree crowns. The SIF signal quantified from sunlit and full-crown pixels was higher than that from 25 m aggregated pixels. The differences were greater for sunlit crown pixels, where the impact of the background was lower. For lower values of crown F_i , the relative contribution of the background for sunlit and full tree crowns increased, and the differences between SIF quantified from crown and aggregated pixels decreased. The F_i of the understory also affected the relationship, with fewer differences observed between SIF quantified from tree crowns and aggregated pixels for the understory with a higher F_i . Fig. 9.c and d show that if we try to calculate the SIF from the crown component based on the relationship between full-tree crowns and aggregated pixels, the increasing of the understory LAI reduces the correlation between them. The highest increase in NRMSE is observed with understory LAI values between 0-1. These results show the contribution of the SIF emitted by the understory not only in the whole scene, but also at the tree-crown level, and illustrate the difficulties in interpreting SIF from coarse resolution images.

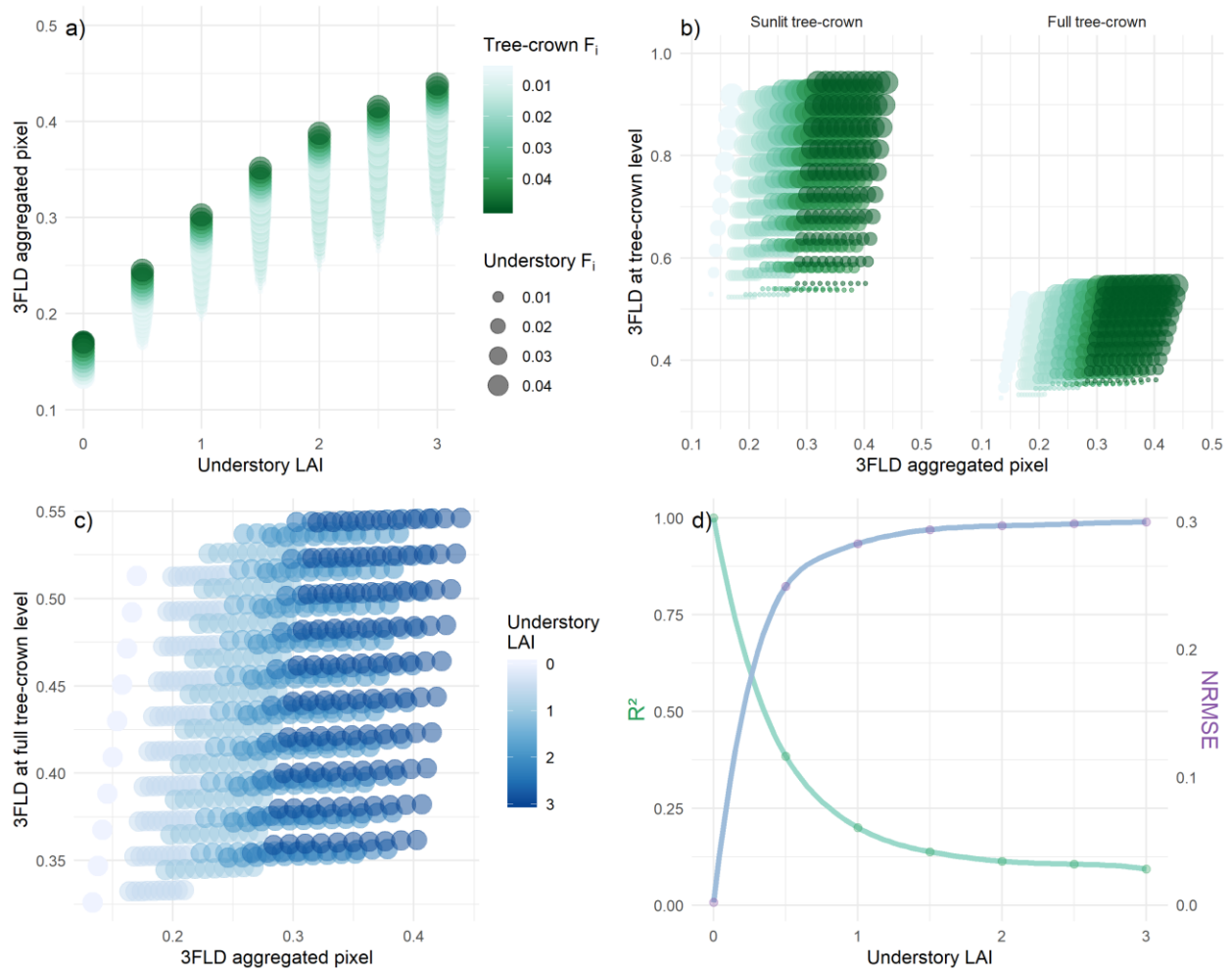


Figure 9. Effects of the variation in fluorescence quantum efficiency (F_i , 0 – 0.05) of the forest understory and the tree crown on the 3FLD ($\text{mW m}^{-2} \text{sr}^{-1} \text{nm}^{-1}$) quantified from 25 m aggregated pixels against the a) understory LAI and b) 3FLD from tree-crowns. Either only the sunlit component (left side) or the entire crown (right side) were aggregated. c) Effects of the variation in LAI (0 – 3) of the forest understory on the relationship between 3FLD calculated from tree-crowns and 25 m aggregated pixels and d) the associated R^2 and NRMSE values for the linear model established for each subgroup of understory LAI.

Based on the proposed modelling approach (Fig. 7), FLIGHT8 was then used to calculate NDVI and 3FLD from aggregated pixels that either did or did not account for the specific contribution of the soil and the understory layer (full or single mode, respectively; Fig. 10). The model simulations and the hyperspectral data were significantly related for NDVI ($R^2 = 0.95$, RMSE =

587 0.04, Fig. 10a) and 3FLD ($R^2 = 0.83$, RMSE = 0.03 mW m⁻² sr⁻¹ nm⁻¹, Fig. 10b) when the model
588 accounted for the contribution of the understory. Similar results were obtained for NDVI using
589 the single-mode model approach, where the specific understory contribution was not considered
590 ($R^2 = 0.96$, RMSE = 0.04, Fig. 10c). However, based on the same assumption, 3FLD was
591 underestimated by the model and the retrieval accuracy was significantly affected ($R^2 = 0.4$,
592 RMSE = 0.28 mW m⁻² sr⁻¹ nm⁻¹, Fig. 10d). These results show the need to consider the
593 contribution of the understory layer in assessing SIF from the aggregated pixels and confirm the
594 ability to use RTM for modelling these effects.

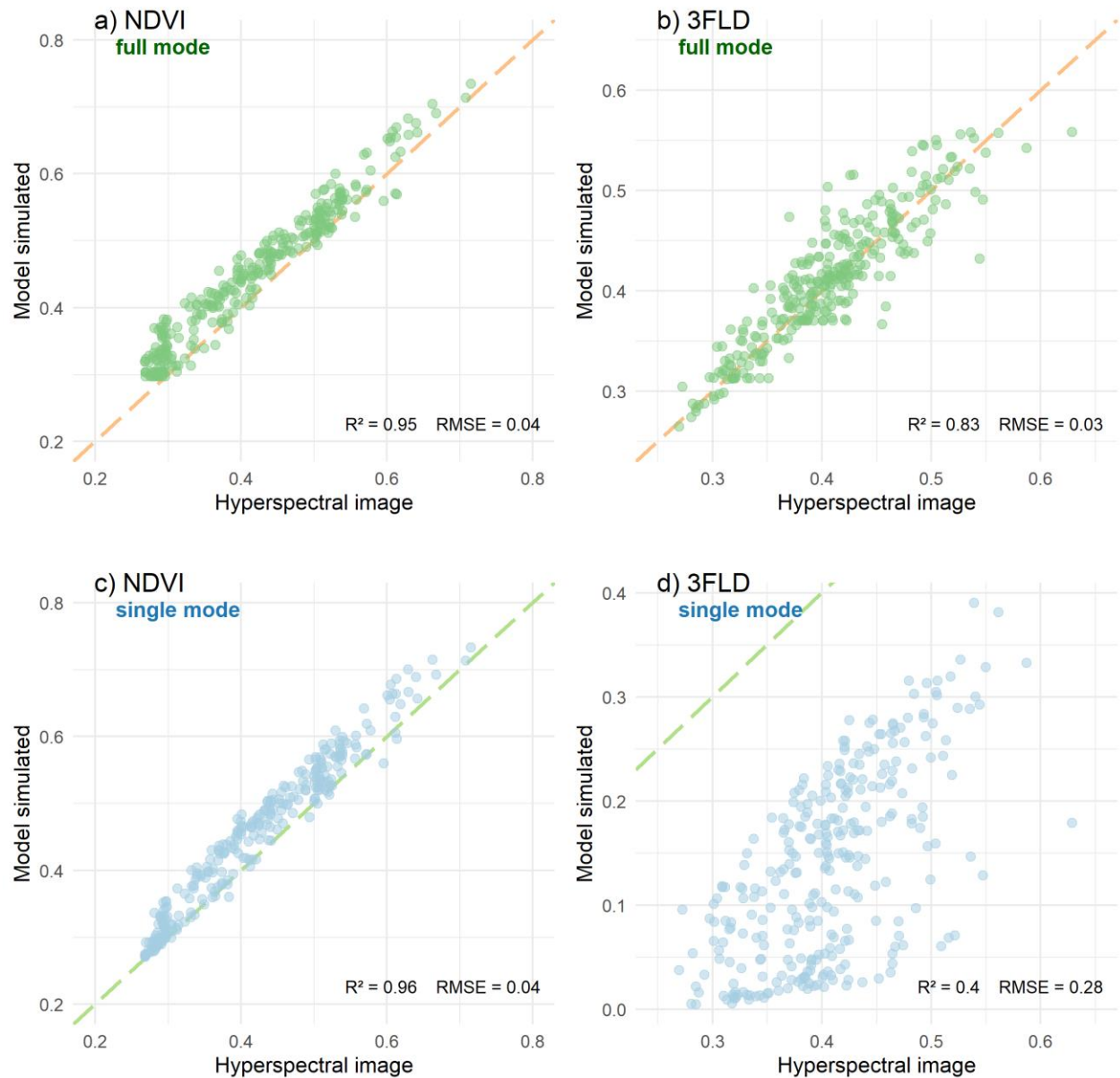


Figure 10. Relationship between hyperspectral data from 25 m aggregated pixels and model-simulated NDVI and 3FLD ($\text{mW m}^{-2} \text{sr}^{-1} \text{nm}^{-1}$) indices accounting for the contribution of SIF of the understory (full mode, *a* and *b*, green points with orange dashed line as 1:1 relationship). The same relationships obtained from model simulations without accounting for the contribution of SIF on the understory and using the empirical reflectance of the background as soil layer (single mode, *c* and *d*, light-blue points with a green dashed line as the identity line).

4. Discussion

The availability of SIF observations from space raises the need to develop and validate new approaches for modelling SIF scattering and re-absorption at the canopy level. The quantification of the fluorescence contribution to top-of-canopy radiance is challenging due to the reduced availability of studies and models with which to interpret the scattering processes within the canopy (Qiu *et al.*, 2019; Romero *et al.*, 2018; Yang and van der Tol, 2018; Zeng *et al.*, 2019). Seeking to fill this gap, the results of this study show the contribution of the SIF emitted by the understory and tree crown components of the total forest canopy. A critical issue found was the selection of a model from among the available ones that can represent the main components of the forest canopy, but that avoids laborious parameterisation that hinders the retrieval of the biophysical properties of the vegetation from images (Hernandez-Clemente *et al.*, 2014). Early attempts at using a 3D-RTM to simulate SIF from heterogeneous canopies (Hernández-Clemente *et al.*, 2017) reported the impact of soil background on the estimation of SIF at the canopy level. Our study introduces a new factor, considering the combined effect of soil and understory vegetation that contributes to the spectral reflectance of the background of an oak grassland at the end of the spring. We used data collected with HyPlant to demonstrate empirically that the understory affects the aggregated pixel values. The higher the aggregation, the more significant were the differences between the pure tree-crown value and the aggregated pixel, and these differences became less relevant at values close to or below the mean crown size. The 3FLD and NDVI quantification were similarly affected by the difference in scale size. Hence, this study demonstrates that the spectral contribution of the understory in heterogeneous canopies might introduce large inaccuracies into measurements calculated from satellite imagery with medium and low spatial resolutions when the quantification of SIF is needed from separated components (tree crowns and understory). This aggregation increases the uncertainties in modelling SIF and

other vegetation indices on a global scale when the spatial distribution and composition of the understory varies over the seasons. In a relatively constant dominant layer (e.g. evergreen canopies), phenological changes of the understory through the season translate into changes in the canopy structure that alter the relationship between GPP and SIF (due to the SIF scattered by the canopy and the re-absorption pattern) (Ahl *et al.*, 2006; Xiaoliang Lu *et al.*, 2018). Even if seasonality remains unchanged, several ecosystems are characterised by a heterogeneous distribution of understory vegetation, which affects the spectral reflectance observed at coarse satellite resolutions. Although this study is carried out with constant values of solar and viewing angles, future work could consider the variation of these parameters. This is possible because FLIGHT8 allows to simulate BRF using different illumination and viewing geometries as it is shown in Fig. S3. Upcoming studies focused on the analysis of the impact of the illumination condition on the quantification of SIF will be very interesting for assessing temporal trends of SIF from different sensors. Another important parameter to consider in that case will be the adjustment of F_i for sunlit and shaded canopies which may vary depending on the short and long term light adaptation of the leaves.

The quantification of SIF emitted by the tree crowns and the understory separately may not always be necessary, in particular for modelling global GPP (Joiner *et al.*, 2014). However, for other studies such as the temporal evolution of photosynthesis related with decay, stress or disease, the physiological state of each component independently should be accurately understood (Stoy *et al.*, 2019). This approach could also be useful for partitioning fluxes of canopy components, which is very challenging from eddy covariance techniques. It is therefore critical that we are able to separate components to take into account the evolution that each of them has over time. The relevance of assessing the contribution of SIF of the understory is

consistent with the model simulation reconstruction from terrestrial laser scanning shown by Liu *et al.* (2019). Future studies should consider the impact of spatial and temporal variations driving global plant dynamics. For these cases, it would be interesting to analyse the sensitivity of these factors on different SIF proxies such as iFLD (Alonso *et al.*, 2008), pFLD (Liu and Liu, 2015), SFM (Mazzoni *et al.*, 2012; Meroni *et al.*, 2010) or NIRv (Badgley *et al.*, 2017; Dechant *et al.*, 2020).

The empirical results of the contribution of SIF emitted by the understory and tree crowns on the quantification of SIF from Hyplant images were in agreement with model simulations. The simulation analysis was performed with a new RTM that includes the option to analyse the contribution of the SIF emitted by the understory and the tree crowns. Although in this work it has not been possible to validate SIF through the RAMI experimental exercises because they are not yet available, RAMI-3 has allowed us to validate the model's ability to represent a new layer. Using a straightforward set of simulations, we show that the higher the LAI of the understory, the smaller the effect of the soil, and therefore, the SIF of the canopy is more similar to the SIF of the scene (Fig. 9), reducing the impact of pixel size variation and scene heterogeneity. However separation of crown and understory is also complicated, and beyond approximately an understory LAI of 0.5 the understory SIF contribution dominates the aggregated pixel. These results are consistent with the significant contribution of the SIF understory to the TOC SIF reported by Liu *et al.* (2019) using an ASD hand-held spectrometer in an open-canopy boreal forest. Based on the need to understand the contribution of the understory at the landscape level, this study shows the accuracy of full tree-crowns SIF calculated from 25m aggregated pixels with the highest increase in NRMSE observed with understory LAI from 0 to 1. These results strengthen the interpretation of the aggregated pixel covered by previous studies in which only the soil effect was taken into

673 account (Hernández-Clemente *et al.*, 2017; Zarco-Tejada *et al.*, 2018). The evaluation of a larger
 674 set of simulations against the airborne imagery (Fig. 10) revealed the capabilities of FLIGHT8 to
 675 model different ecosystem components. The comparison between airborne and model-simulated
 676 retrievals showed different effects on NDVI and 3FLD under the two proposed approaches:
 677 model simulations that included only one layer as background (single-mode) or those that
 678 accounted for the specific contribution of soil and understory layers (full-mode). The relationship
 679 between model-simulated and airborne NDVI was similar ($R^2 = 0.95$, RMSE = 0.04) in both cases
 680 (Fig. 10 a, c). This result was predictable as the presence of soil and vegetation cover is included
 681 in both approaches. In full-mode simulations, we account for the contribution of two different
 682 layers, understory and soil (Fig. 10 a). In single-mode simulations, the layer of the soil is the
 683 spectral response of the background extracted from an image with a pixel size of 1.5 m in which
 684 both components (soil and vegetation) are mixed (Fig. 10 c). The main difference was observed
 685 in the quantification of SIF, as model simulations in single mode do not take into account the
 686 fluorescence emission of the understory. In this case, the relationship between airborne and
 687 model-simulated 3FLD significantly improved using FLIGHT8 in full mode ($R^2 = 0.83$, RMSE
 688 = $0.03 \text{ mW m}^{-2}\text{sr}^{-1}\text{nm}^{-1}$) in comparison with simulations performed in single mode ($R^2 = 0.4$,
 689 RMSE = $0.28 \text{ mW m}^{-2}\text{sr}^{-1}\text{nm}^{-1}$) (Fig. 10. b, d), because the canopy model does not include the
 690 understory contribution of the fluorescence emission in single mode. The results demonstrated
 691 that understory SIF could substantially contribute to the total canopy SIF quantified from
 692 aggregated pixels in open-canopy forests. Moreover, FLIGHT8 can be used to resolve the
 693 problem of interpreting information on a large scale when the effect of the understory plays a
 694 fundamental role, such as in tree-grass ecosystems or open forests.

The heterogeneous spatial distribution of trees and understory layers in the landscape is one of the main factors that inherently introduces uncertainty into the retrieval of biophysical parameters of vegetation through models (Eriksson *et al.*, 2006; Yu *et al.*, 2018). The estimation of these parameters simultaneously contains many implications for the recovery of GPP (Li *et al.*, 2018) and even the interpretation of GPP using SIF as a proxy varies greatly depending on the type of cover (Tagliabue *et al.*, 2019). This study highlights the need for a solution that allows the contribution of the understory in aggregated pixels and its impact on the fluorescence estimation of the total canopy to be modelled. Future studies should also take into account the vertical variability of the maximum rate of carboxylation (V_{cmax}), which has been proven to be a key parameter for estimation CO_2 assimilation in crops (Camino *et al.*, 2019) and the xanthophyll cycle included in the extended version of Fluspect (Vilfan *et al.*, 2018).

The results of this study contribute to understanding how the quantification of SIF from aggregated pixels can be improved for mixed tree, grass and woodland ecosystems, which cover a large part of the globe (up to 33% according to Hanan and Hill (2012)). The understory of Mediterranean oak woodlands is mainly covered by grasslands, where light availability and nutrient-induced changes alter plant functional traits and canopy structure and control the relationship between GPP and SIF (Migliavacca *et al.*, 2017). However, in other types of ecosystems with higher density, the contribution of the understory may be different. Hence, future efforts should focus on assessing the contribution of the SIF emitted by the understory in the quantification of total canopy SIF in other types of ecosystems and forest complexities. These studies will be decisive for the ability to measure and interpret SIF at the global scale.

5. Conclusions

The results presented here demonstrate that the fluorescence signal calculated from medium spatial resolution is significantly affected by variations in the understory. The contribution of understory SIF increased rapidly with understory LAI values, dominating the total scene SIF for LAI greater than 0.5. Beyond this range, the correlation strength of crown SIF with aggregated pixel SIF reduces, requiring modelling of the system if separation of crown and understory SIF is necessary, for example in assessing forest health or seasonality. Thus, the use of medium- to low-resolution images for assessing the physiological condition of forest and agricultural canopies requires taking into account the contribution of the SIF emitted by the understory when working with heterogeneous ecosystems.

This study demonstrates the need to include the contribution of SIF emitted by the understory in the interpretation of SIF emitted by forest canopies with RTM approaches. The use of FLIGHT8, which integrates the effect of fluorescence (FluorFLIGHT), has allowed a new model to be developed that takes into account the effect of the understory to model SIF signals and discriminate this information in each of its components. The model has been tested by intercomparison with other models and validated empirically using high spatial and spectral resolution imagery. Due to its spatial variability throughout, our study area enabled comprehensive evaluation. Multitemporal analysis of the impact of phenological changes of the understory over the vegetation canopy is beyond the scope of this study but will be the central topic of a follow-up contribution.

The results suggest that this model could be used to improve the interpretation of SIF at the tree canopy level when we need to separate between different aggregated components and account for the background effects. The ability to quantify SIF from coarse resolution images is a further

advantage for quantification of the model at a global scale. Future studies should be focused on the potential use of 3D-RTM to provide information at a high-spectral resolution and frequency from current and future satellite missions as OCO-2, TROPOMI or FLEX-Sentinel.

Acknowledgements

Data collection was partially supported by SynerTGE CGL2015-G9095-R (MINECO/FEDER, UE) and the ESA-FLEX Sense 2018 Project (ESA Contract No. ESA RFP/3-15477/18/NL/NA). A. Hornero was supported by research fellowship DTC GEO 29 “Detection of global photosynthesis and forest health from space” from the Science Doctoral Training Centre (Swansea University, United Kingdom). P. North was supported by the NERC National Centre for Earth Observation (United Kingdom). The authors would also like to thank Bastian Siegmann and Patrick Rademske from the Institute of Bio- and Geosciences (Forschungszentrum Jülich GmbH, Germany) for laboratory assistance and the support provided during the airborne campaigns. We thank Sergio Cogliati (Università degli Studi di Milano-Bicocca, Italy) and Alexander Damm (University of Zurich, Switzerland) for scientific discussions. We also thank Javier Pacheco-Labrador, David Martini and Tarek El-Madany (Max Planck Institute for Biogeochemistry, Germany), Arnaud Carrara (Fundación CEAM, Spain), Karolina Sakowska (National Research Council, Italy) as well as SpecLab personnel (Spanish National Research Council, Spain) for their support during the field campaigns at the Majadas de Tiétar research station. All the figures included in this manuscript have been designed to include colour schemes suitable for people with visual disabilities and in view of printing considerations (Harrower and Brewer, 2003).

Appendix A. Supplementary material

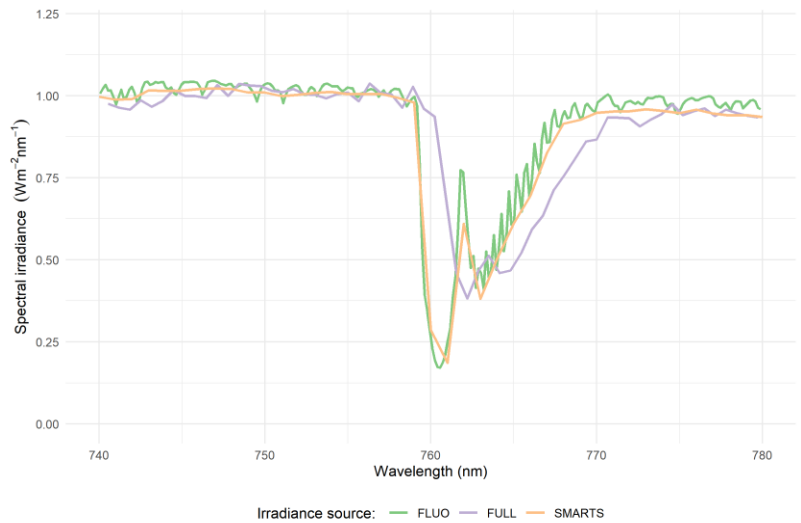


Figure S1. Comparison between different sources of solar irradiance information.

Table S1

Input range for FLIGHT8 according to the model intercomparison.

Simulation*	Parameters	Solar Zenith Angle (deg)	Scattered Radius (m)	Leaf Area Index (m ² m ⁻²)	Canopy Height (m)	Leaf Angle Distribution	Leaf ρ/τ (%)	Soil ρ (%)
HOM01,TUR,ERE,NR1,00	0	0	1	1	Erectophile	0.5/0.5	1.0	
HOM03,DIS,ERE,RED,50	50	0.05	3	2	Erectophile	0.0546/ 0.0149	0.127	
HOM05,TUR,ERE,NR1,60	60	0	5	1	Erectophile	0.5/0.5	1.0	
HOM12,DIS,ERE,NR1,30	30	0.05	2	1	Erectophile	0.5/0.5	1.0	
HOM13,DIS,PLA,RED,20	20	0.1	3	2	Planophile	0.0546/ 0.0149	0.127	
HOM03,TUR,UNI,NIR,20	20	0	3	1	Uniform	0.4957/ 0.4409	0.159	

* HOM (Homogeneous)

TUR (Turbid), DIS (Discrete)

ERE (Erectophile), PLA (Planophile), UNI (Uniform)

NR1 (Purist corner), RED (Red, solar domain), NIR (Near-infrared, solar domain)

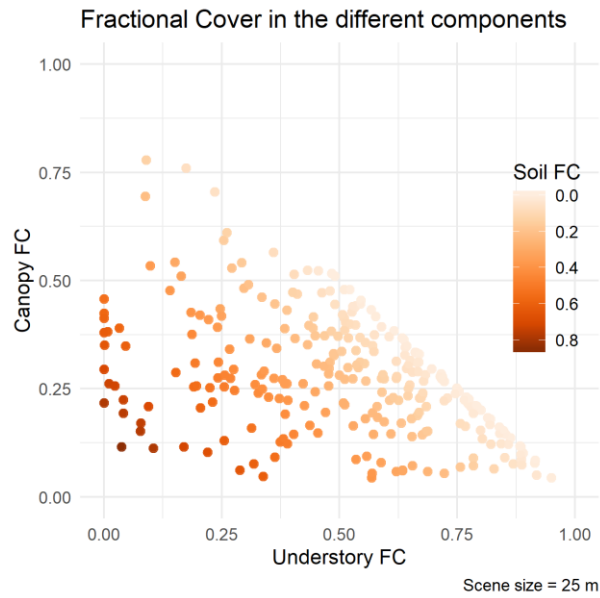
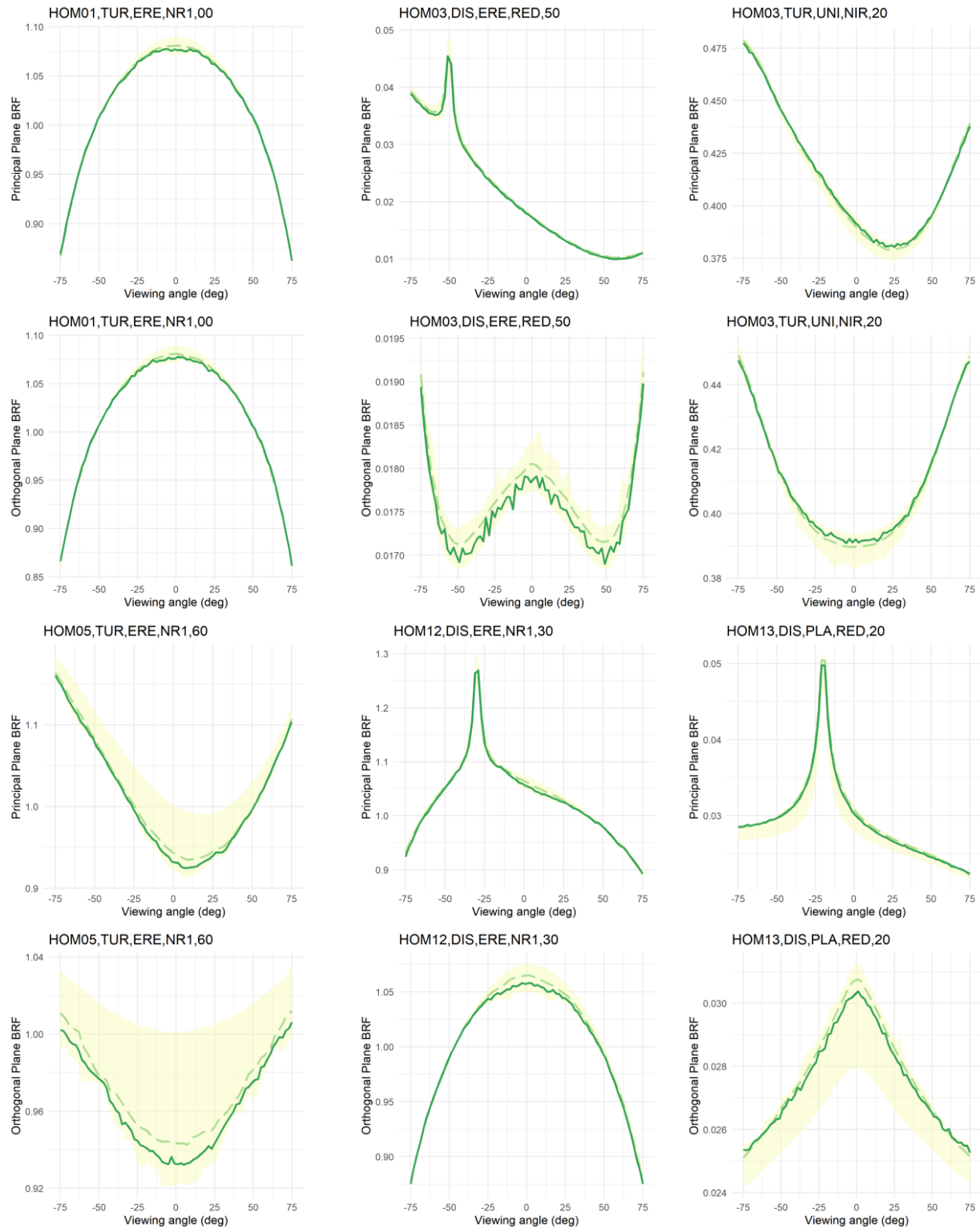


Figure S2. Example of the contribution of scene components for a 25 m window based on the relationship between canopy and understory fractional cover (FC) and soil FC shown as different intensity orange points.



775

776 **Figure S3.** Comparison of FLIGHT8 with other RTMs using the set of scenarios proposed by the
 777 RAMI intercomparison exercise. The results of RAMIREF are shown by the dashed light-green
 778 line and those from other models within the shaded area.

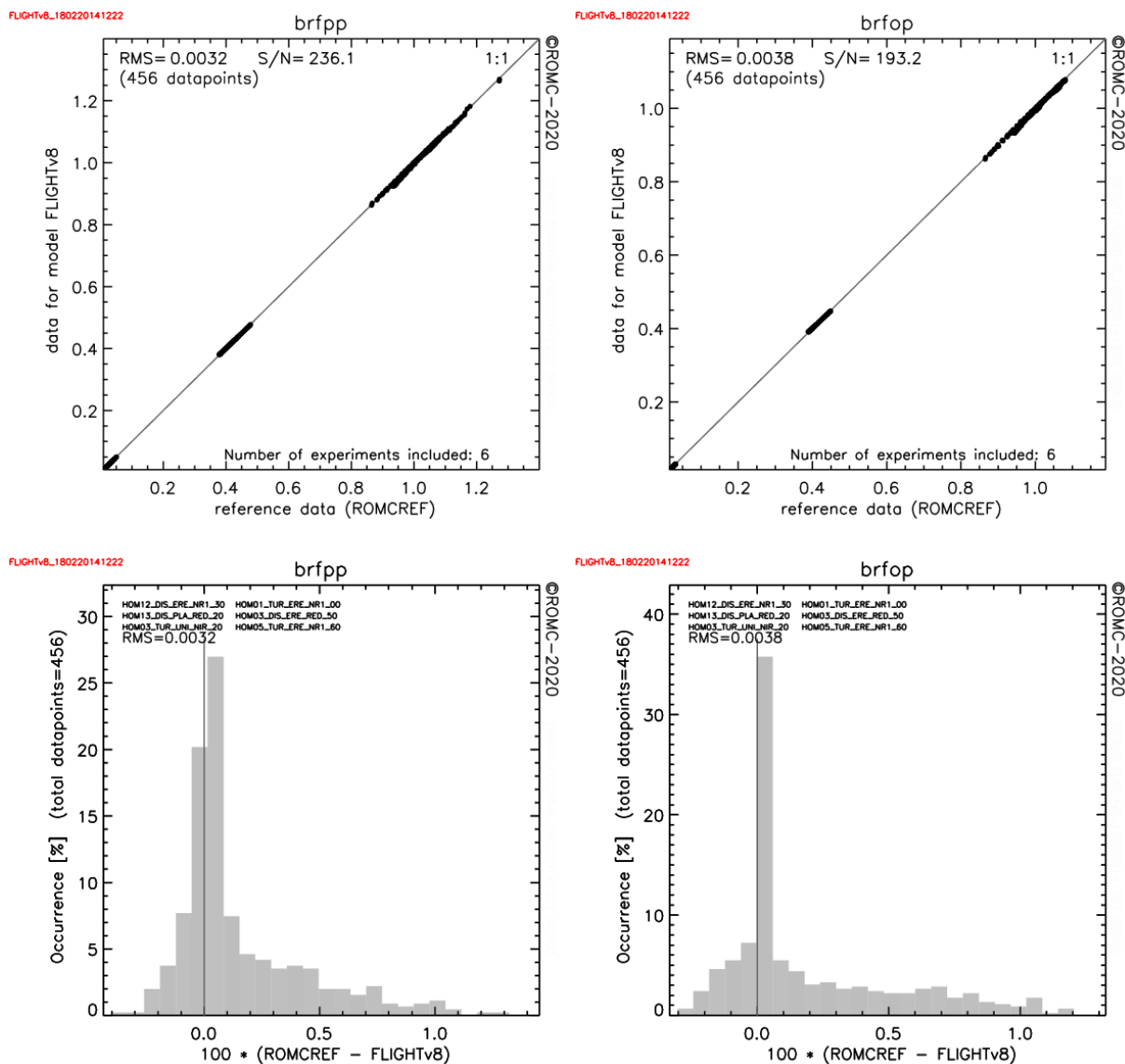


Figure S4. Global bi-directional reflectance factor 1-to-1 comparison (top) and histogram differences (bottom) for principal (left) and orthogonal planes (right) within the ROMC-generated results.

784 **References**

- 785 Ahl, D.E., Gower, S.T., Burrows, S.N., Shabanov, N.V., Myneni, R.B., Knyazikhin, Y., 2006.
786 Monitoring spring canopy phenology of a deciduous broadleaf forest using MODIS.
787 Remote Sens. Environ. 104, 88–95. <https://doi.org/10.1016/j.rse.2006.05.003>
- 788 Alonso, L., Gomez-Chova, L., Vila-Frances, J., Amoros-Lopez, J., Guanter, L., Calpe, J.,
789 Moreno, J., 2008. Improved Fraunhofer Line Discrimination Method for Vegetation
790 Fluorescence Quantification. IEEE Geosci. Remote Sens. Lett. 5, 620–624.
791 <https://doi.org/10.1109/LGRS.2008.2001180>
- 792 Atherton, J., Liu, W., Porcar-Castell, A., 2019. Nocturnal Light Emitting Diode Induced
793 Fluorescence (LEDIF): A new technique to measure the chlorophyll a fluorescence
794 emission spectral distribution of plant canopies in situ. Remote Sens. Environ. 231,
795 111137. <https://doi.org/10.1016/j.rse.2019.03.030>
- 796 Badgley, G., Field, C.B., Berry, J.A., 2017. Canopy near-infrared reflectance and terrestrial
797 photosynthesis. Sci. Adv. 3, e1602244. <https://doi.org/10.1126/sciadv.1602244>
- 798 Bogdanovich, E., Perez-Priego, O., El-Madany, T.S., Guderle, M., Pacheco-Labrador, J., Levick,
799 S.R., Moreno, G., Carrara, A., Pilar Martin, M., Migliavacca, M., submitted. Using
800 Terrestrial Laser Scanning for characterizing tree structural parameters and their changes
801 under different management in a Mediterranean open woodland.
- 802 Bye, I.J., North, P.R.J., Los, S.O., Kljun, N., Rosette, J.A.B., Hopkinson, C., Chasmer, L.,
803 Mahoney, C., 2017. Estimating forest canopy parameters from satellite waveform LiDAR
804 by inversion of the FLIGHT three-dimensional radiative transfer model. Remote Sens.
805 Environ. 188, 177–189. <https://doi.org/10.1016/j.rse.2016.10.048>
- 806 Camino, C., Gonzalez-Dugo, V., Hernandez, P., Zarco-Tejada, P.J., 2019. Radiative transfer
807 Vcmax estimation from hyperspectral imagery and SIF retrievals to assess photosynthetic
808 performance in rainfed and irrigated plant phenotyping trials. Remote Sens. Environ. 231,
809 111186. <https://doi.org/10.1016/j.rse.2019.05.005>
- 810 Celesti, M., Biriukova, K., Campbell, P.K.E., Cesana, I., Cogliati, S., Damm, A., Drusch, M.,
811 Julitta, T., Middleton, E., Migliavacca, M., Miglietta, F., Panigada, C., Rascher, U.,
812 Rossini, M., Schuettemeyer, D., Tagliabue, G., van der Tol, C., Verrelst, J., Yang, P.,
813 Colombo, R., 2019. Exploring continuous time series of vegetation hyperspectral
814 reflectance and solar-induced fluorescence through radiative transfer model inversion.
815 Presented at the AGU Fall Meeting 2019, AGU.
- 816 Cendrero-Mateo, M.P., Moran, M.S., Papuga, S.A., Thorp, K.R., Alonso, L., Moreno, J., Ponce-
817 Campos, G., Rascher, U., Wang, G., 2016. Plant chlorophyll fluorescence: active and
818 passive measurements at canopy and leaf scales with different nitrogen treatments. J. Exp.
819 Bot. 67, 275–286. <https://doi.org/10.1093/jxb/erv456>
- 820 Damm, A., Guanter, L., Paul-Limoges, E., van der Tol, C., Hueni, A., Buchmann, N., Eugster,
821 W., Ammann, C., Schaepman, M.E., 2015. Far-red sun-induced chlorophyll fluorescence
822 shows ecosystem-specific relationships to gross primary production: An assessment based
823 on observational and modeling approaches. Remote Sens. Environ. 166, 91–105.
824 <https://doi.org/10.1016/j.rse.2015.06.004>
- 825 Dechant, B., Ryu, Y., Badgley, G., Zeng, Y., Berry, J.A., Zhang, Y., Goulas, Y., Li, Z., Zhang,
826 Q., Kang, M., Li, J., Moya, I., 2020. Canopy structure explains the relationship between
827 photosynthesis and sun-induced chlorophyll fluorescence in crops. Remote Sens. Environ.
828 241, 111733. <https://doi.org/10.1016/j.rse.2020.111733>

- Duveiller, G., Filipponi, F., Walther, S., Köhler, P., Frankenberg, C., Guanter, L., Cescatti, A., 2020. A spatially downscaled sun-induced fluorescence global product for enhanced monitoring of vegetation productivity. *Earth Syst. Sci. Data* 12, 1101–1116. <https://doi.org/10.5194/essd-12-1101-2020>
- Eriksson, H.M., Eklundh, L., Kuusk, A., Nilson, T., 2006. Impact of understory vegetation on forest canopy reflectance and remotely sensed LAI estimates. *Remote Sens. Environ.* 103, 408–418. <https://doi.org/10.1016/j.rse.2006.04.005>
- Feret, J.-B., François, C., Asner, G.P., Gitelson, A.A., Martin, R.E., Bidel, L.P.R., Ustin, S.L., le Maire, G., Jacquemoud, S., 2008. PROSPECT-4 and 5: Advances in the leaf optical properties model separating photosynthetic pigments. *Remote Sens. Environ.* 112, 3030–3043. <https://doi.org/10.1016/j.rse.2008.02.012>
- Frankenberg, C., Fisher, J.B., Worden, J., Badgley, G., Saatchi, S.S., Lee, J.-E., Toon, G.C., Butz, A., Jung, M., Kuze, A., Yokota, T., 2011. New global observations of the terrestrial carbon cycle from GOSAT: Patterns of plant fluorescence with gross primary productivity. *Geophys. Res. Lett.* 38, L17706. <https://doi.org/10.1029/2011GL048738>
- Gastellu-Etchegorry, J., Lauret, N., Yin, T., Landier, L., Kallel, A., Malenovsky, Z., Bitar, A.A., Aval, J., Benhmida, S., Qi, J., Medjdoub, G., Guilleux, J., Chavanon, E., Cook, B., Morton, D., Chrysoulakis, N., Mitraka, Z., 2017. DART: Recent Advances in Remote Sensing Data Modeling With Atmosphere, Polarization, and Chlorophyll Fluorescence. *IEEE J. Sel. Top. Appl. Earth Obs. Remote Sens.* 10, 2640–2649. <https://doi.org/10.1109/JSTARS.2017.2685528>
- Gastellu-Etchegorry, J.P., Demarez, V., Pinel, V., Zagolski, F., 1996. Modeling radiative transfer in heterogeneous 3-D vegetation canopies. *Remote Sens. Environ.* 58, 131–156. [https://doi.org/10.1016/0034-4257\(95\)00253-7](https://doi.org/10.1016/0034-4257(95)00253-7)
- Gonzalez-Cascon, M. del R., Jiménez, L.S., Fillola, I.V., Santafe, M.M., 2017. Aqueous-acetone extraction improves the drawbacks of using dimethylsulfoxide as solvent for photometric pigment quantification in *Quercus ilex* leaves. *For. Syst.* 26, 5.
- Gonzalez-Cascon, R., Martin, M.P., 2018. Protocol for pigment content quantification in herbaceous covers: sampling and analysis. *Life Sci. Protoc. Repos. Protoc.* <https://doi.org/10.17504/protocols.io.qs6dwhe>
- Govaerts, Y.M., Verstraete, M.M., 1998. Raytran: a Monte Carlo ray-tracing model to compute light scattering in three-dimensional heterogeneous media. *IEEE Trans. Geosci. Remote Sens.* 36, 493–505. <https://doi.org/10.1109/36.662732>
- Guanter, L., Frankenberg, C., Dudhia, A., Lewis, P.E., Gómez-Dans, J., Kuze, A., Suto, H., Grainger, R.G., 2012. Retrieval and global assessment of terrestrial chlorophyll fluorescence from GOSAT space measurements. *Remote Sens. Environ.* 121, 236–251. <https://doi.org/10.1016/j.rse.2012.02.006>
- Gueymard, C., 1995. SMARTS2: a simple model of the atmospheric radiative transfer of sunshine: algorithms and performance assessment. Florida Solar Energy Center Cocoa, FL.
- Gueymard, C.A., 2001. Parameterized transmittance model for direct beam and circumsolar spectral irradiance. *Sol. Energy* 71, 325–346. [https://doi.org/10.1016/S0038-092X\(01\)00054-8](https://doi.org/10.1016/S0038-092X(01)00054-8)
- Guillen-Climent, M.L., Zarco-Tejada, P.J., Berni, J.A.J., North, P.R.J., Villalobos, F.J., 2012. Mapping radiation interception in row-structured orchards using 3D simulation and high-resolution airborne imagery acquired from a UAV. *Precis. Agric.* 13, 473–500. <https://doi.org/10.1007/s11119-012-9263-8>

- Hanan, N.P., Hill, M.J., 2012. Savannas in a Changing Earth System. The NASA Terrestrial Ecology Tree-Grass Project (Commissioned White Paper submitted to NASA Terrestrial Ecology Program). South Dakota State University and The University of North Dakota.
- Harrower, M., Brewer, C.A., 2003. ColorBrewer. org: an online tool for selecting colour schemes for maps. *Cartogr. J.* 40, 27–37.
- Hernandez-Clemente, R., Navarro-Cerrillo, R.M., Zarco-Tejada, P.J., 2014. Deriving Predictive Relationships of Carotenoid Content at the Canopy Level in a Conifer Forest Using Hyperspectral Imagery and Model Simulation. *IEEE Trans. Geosci. Remote Sens.* 52, 5206–5217. <https://doi.org/10.1109/TGRS.2013.2287304>
- Hernández-Clemente, R., North, P.R.J., Hornero, A., Zarco-Tejada, P.J., 2017. Assessing the effects of forest health on sun-induced chlorophyll fluorescence using the FluorFLIGHT 3-D radiative transfer model to account for forest structure. *Remote Sens. Environ.* 193, 165–179. <https://doi.org/10.1016/j.rse.2017.02.012>
- Hernandez-Clemente, R., North, P.R.J., Hornero, A., Zarco-Tejada, P.J., 2017. Assessing potential of sun-induced chlorophyll fluorescence for early detection of forest decline using a 3-D radiative transfer model accounting for forest structure, in: *Recent Advances in Quantitative Remote Sensing*. Sobrino, J.A., Valencia.
- Holben, B.N., Eck, T.F., Slutsker, I., Tanré, D., Buis, J.P., Setzer, A., Vermote, E., Reagan, J.A., Kaufman, Y.J., Nakajima, T., Lavenu, F., Jankowiak, I., Smirnov, A., 1998. AERONET—A Federated Instrument Network and Data Archive for Aerosol Characterization. *Remote Sens. Environ.* 66, 1–16. [https://doi.org/10.1016/S0034-4257\(98\)00031-5](https://doi.org/10.1016/S0034-4257(98)00031-5)
- Hornero, A., Hernández-Clemente, R., North, P.R.J., Beck, P.S.A., Boscia, D., Navas-Cortes, J.A., Zarco-Tejada, P.J., 2020. Monitoring the incidence of *Xylella fastidiosa* infection in olive orchards using ground-based evaluations, airborne imaging spectroscopy and Sentinel-2 time series through 3-D radiative transfer modelling. *Remote Sens. Environ.* 236, 111480. <https://doi.org/10.1016/j.rse.2019.111480>
- Jacquemoud, S., Baret, F., 1990. PROSPECT: A model of leaf optical properties spectra. *Remote Sens. Environ.* 34, 75–91. [https://doi.org/10.1016/0034-4257\(90\)90100-Z](https://doi.org/10.1016/0034-4257(90)90100-Z)
- Joiner, J., Yoshida, Y., Vasilkov, A.P., Schaefer, K., Jung, M., Guanter, L., Zhang, Y., Garrity, S., Middleton, E.M., Huemmrich, K.F., Gu, L., Beileli Marchesini, L., 2014. The seasonal cycle of satellite chlorophyll fluorescence observations and its relationship to vegetation phenology and ecosystem atmosphere carbon exchange. *Remote Sens. Environ.* 152, 375–391. <https://doi.org/10.1016/j.rse.2014.06.022>
- Joiner, J., Yoshida, Y., Vasilkov, A.P., Yoshida, Y., Corp, L.A., Middleton, E.M., 2011. First observations of global and seasonal terrestrial chlorophyll fluorescence from space. *Biogeosciences* 8, 637–651. <https://doi.org/10.5194/bg-8-637-2011>
- Kallel, A., 2020. FluLCVRT: Reflectance and fluorescence of leaf and canopy modeling based on Monte Carlo vector radiative transfer simulation. *J. Quant. Spectrosc. Radiat. Transf.* 253, 107183. <https://doi.org/10.1016/j.jqsrt.2020.107183>
- Kobayashi, H., Ryu, Y., Baldocchi, D.D., Welles, J.M., Norman, J.M., 2013. On the correct estimation of gap fraction: How to remove scattered radiation in gap fraction measurements? *Agric. For. Meteorol.* 174–175, 170–183. <https://doi.org/10.1016/j.agrformet.2013.02.013>
- Köhler, P., Frankenberg, C., Magney, T., Guanter, L., Joanna, J., Landgraf, J., 2018. Global Retrievals of Solar-Induced Chlorophyll Fluorescence With TROPOMI: First Results and

- Intersensor Comparison to OCO-2. *Geophys. Res. Lett.* 45.
<https://doi.org/10.1029/2018GL079031>
- Lewis, P., 1999. Three-dimensional plant modelling for remote sensing simulation studies using the Botanical Plant Modelling System. *Agronomie* 19, 185–210.
<https://doi.org/10.1051/agro:19990302>
- Li, X., Xiao, J., He, B., Arain, M.A., Beringer, J., Desai, A.R., Emmel, C., Hollinger, D.Y., Krasnova, A., Mammarella, I., Noe, S.M., Ortiz, P.S., Rey- Sanchez, A.C., Rocha, A.V., Varlagin, A., 2018. Solar-induced chlorophyll fluorescence is strongly correlated with terrestrial photosynthesis for a wide variety of biomes: First global analysis based on OCO-2 and flux tower observations. *Glob. Change Biol.* 24, 3990–4008.
<https://doi.org/10.1111/gcb.14297>
- Lin, S., Li, J., Liu, Q., Huete, A., Li, L., 2018. Effects of Forest Canopy Vertical Stratification on the Estimation of Gross Primary Production by Remote Sensing. *Remote Sens.* 10, 1329.
<https://doi.org/10.3390/rs10091329>
- Liu, L., Liu, X., Hu, J., 2015. Effects of spectral resolution and SNR on the vegetation solar-induced fluorescence retrieval using FLD-based methods at canopy level. *Eur. J. Remote Sens.* 48, 743–762. <https://doi.org/10.5721/EuJRS20154841>
- Liu, W., Atherton, J., Möttus, M., Gastellu-Etchegorry, J.-P., Malenovský, Z., Raunonen, P., Åkerblom, M., Mäkipää, R., Porcar-Castell, A., 2019. Simulating solar-induced chlorophyll fluorescence in a boreal forest stand reconstructed from terrestrial laser scanning measurements. *Remote Sens. Environ.* 232, 111274.
<https://doi.org/10.1016/j.rse.2019.111274>
- Liu, X., Liu, L., 2015. Improving Chlorophyll Fluorescence Retrieval Using Reflectance Reconstruction Based on Principal Components Analysis. *IEEE Geosci. Remote Sens. Lett.* 12, 1645–1649. <https://doi.org/10.1109/LGRS.2015.2417857>
- Liu, X., Liu, L., 2014. Assessing Band Sensitivity to Atmospheric Radiation Transfer for Space-Based Retrieval of Solar-Induced Chlorophyll Fluorescence. *Remote Sens.* 6, 10656–10675. <https://doi.org/10.3390/rs61110656>
- Lu, Xincheng, Cheng, X., Li, X., Tang, J., 2018. Opportunities and challenges of applications of satellite-derived sun-induced fluorescence at relatively high spatial resolution. *Sci. Total Environ.* 619–620, 649–653. <https://doi.org/10.1016/j.scitotenv.2017.11.158>
- Lu, Xiaoliang, Liu, Z., Zhou, Y., Liu, Y., An, S., Tang, J., 2018. Comparison of Phenology Estimated from Reflectance-Based Indices and Solar-Induced Chlorophyll Fluorescence (SIF) Observations in a Temperate Forest Using GPP-Based Phenology as the Standard. *Remote Sens.* 10, 932. <https://doi.org/10.3390/rs10060932>
- Maier, S.W., Günther, K.P., Stellmes, M., 2003. Sun-Induced Fluorescence: A New Tool for Precision Farming. *Digit. Imaging Spectr. Tech. Appl. Precis. Agric. Crop Physiol. aspecialpubli*, 209–222. <https://doi.org/10.2134/asaspecpub66.c16>
- Malenovský, Z., Homolová, L., Lukeš, P., Buddenbaum, H., Verrelst, J., Alonso, L., Schaepman, M.E., Lauret, N., Gastellu-Etchegorry, J.-P., 2019. Variability and Uncertainty Challenges in Scaling Imaging Spectroscopy Retrievals and Validations from Leaves Up to Vegetation Canopies. *Surv. Geophys.* 40, 631–656. <https://doi.org/10.1007/s10712-019-09534-y>
- Markiet, V., Möttus, M., 2020. Estimation of boreal forest floor reflectance from airborne hyperspectral data of coniferous forests. *Remote Sens. Environ.* 249, 112018.
<https://doi.org/10.1016/j.rse.2020.112018>

968 Mazzoni, M., Meroni, M., Fortunato, C., Colombo, R., Verhoef, W., 2012. Retrieval of maize
969 canopy fluorescence and reflectance by spectral fitting in the O₂-A absorption band.
970 *Remote Sens. Environ.* 124, 72–82. <https://doi.org/10.1016/j.rse.2012.04.025>

971 Melendo-Vega, J.R., Martín, M.P., Pacheco-Labrador, J., González-Cascón, R., Moreno, G.,
972 Pérez, F., Migliavacca, M., García, M., North, P., Riaño, D., 2018. Improving the
973 Performance of 3-D Radiative Transfer Model FLIGHT to Simulate Optical Properties of
974 a Tree-Grass Ecosystem. *Remote Sens.* 10, 2061. <https://doi.org/10.3390/rs10122061>

975 Mendiguren, G., Pilar Martín, M., Nieto, H., Pacheco-Labrador, J., Jurdao, S., 2015. Seasonal
976 variation in grass water content estimated from proximal sensing and MODIS time series
977 in a Mediterranean Fluxnet site. *Biogeosciences* 12, 5523–5535.
978 <https://doi.org/10.5194/bg-12-5523-2015>

979 Meng, R., Dennison, P.E., Zhao, F., Shendryk, I., Rickert, A., Hanavan, R.P., Cook, B.D., Serbin,
980 S.P., 2018. Mapping canopy defoliation by herbivorous insects at the individual tree level
981 using bi-temporal airborne imaging spectroscopy and LiDAR measurements. *Remote*
982 *Sens. Environ.* 215, 170–183. <https://doi.org/10.1016/j.rse.2018.06.008>

983 Meroni, M., Busetto, L., Colombo, R., Guanter, L., Moreno, J., Verhoef, W., 2010. Performance
984 of Spectral Fitting Methods for vegetation fluorescence quantification. *Remote Sens.*
985 *Environ.* 114, 363–374. <https://doi.org/10.1016/j.rse.2009.09.010>

986 Migliavacca, M., Perez- Priego, O., Rossini, M., El- Madany, T.S., Moreno, G., van der Tol, C.,
987 Rascher, U., Berninger, A., Bessenbacher, V., Burkart, A., Carrara, A., Fava, F., Guan, J.-
988 H., Hammer, T.W., Henkel, K., Juarez- Alcalde, E., Julitta, T., Kolle, O., Martín, M.P.,
989 Musavi, T., Pacheco- Labrador, J., Pérez- Burgueño, A., Wutzler, T., Zaehle, S.,
990 Reichstein, M., 2017. Plant functional traits and canopy structure control the relationship
991 between photosynthetic CO₂ uptake and far-red sun-induced fluorescence in a
992 Mediterranean grassland under different nutrient availability. *New Phytol.* 214, 1078–
993 1091. <https://doi.org/10.1111/nph.14437>

994 Mohammed, G.H., Colombo, R., Middleton, E.M., Rascher, U., van der Tol, C., Nedbal, L.,
995 Goulas, Y., Pérez-Priego, O., Damm, A., Meroni, M., Joiner, J., Cogliati, S., Verhoef, W.,
996 Malenovsky, Z., Gastellu-Etchegorry, J.-P., Miller, J.R., Guanter, L., Moreno, J., Moya,
997 I., Berry, J.A., Frankenberg, C., Zarco-Tejada, P.J., 2019. Remote sensing of solar-
998 induced chlorophyll fluorescence (SIF) in vegetation: 50 years of progress. *Remote Sens.*
999 *Environ.* 231, 111177. <https://doi.org/10.1016/j.rse.2019.04.030>

1000 Montesano, P.M., Rosette, J., Sun, G., North, P., Nelson, R.F., Dubayah, R.O., Ranson, K.J.,
1001 Kharuk, V., 2015. The uncertainty of biomass estimates from modeled ICESat-2 returns
1002 across a boreal forest gradient. *Remote Sens. Environ.* 158, 95–109.
1003 <https://doi.org/10.1016/j.rse.2014.10.029>

1004 North, P.R.J., 1996. Three-dimensional forest light interaction model using a Monte Carlo
1005 method. *IEEE Trans. Geosci. Remote Sens.* 34, 946–956.
1006 <https://doi.org/10.1109/36.508411>

1007 North, P.R.J., Rosette, J.A.B., Suárez, J.C., Los, S.O., 2010. A Monte Carlo radiative transfer
1008 model of satellite waveform LiDAR. *Int. J. Remote Sens.* 31, 1343–1358.
1009 <https://doi.org/10.1080/01431160903380664>

1010 Pedrós, R., Goulas, Y., Jacquemoud, S., Louis, J., Moya, I., 2010. FluorMODleaf: A new leaf
1011 fluorescence emission model based on the PROSPECT model. *Remote Sens. Environ.*
1012 114, 155–167. <https://doi.org/10.1016/j.rse.2009.08.019>

- Plascyk, J.A., 1975. The MK II Fraunhofer Line Discriminator (FLD-II) for Airborne and Orbital Remote Sensing of Solar-Stimulated Luminescence. *Opt. Eng.* 14, 144339. <https://doi.org/10.1117/12.7971842>
- Qiu, B., Chen, J.M., Ju, W., Zhang, Q., Zhang, Y., 2019. Simulating emission and scattering of solar-induced chlorophyll fluorescence at far-red band in global vegetation with different canopy structures. *Remote Sens. Environ.* 233, 111373. <https://doi.org/10.1016/j.rse.2019.111373>
- Rascher, U., Alonso, L., Burkart, A., Cilia, C., Cogliati, S., Colombo, R., Damm, A., Drusch, M., Guanter, L., Hanus, J., Hyvärinen, T., Julitta, T., Jussila, J., Kataja, K., Kokkalis, P., Kraft, S., Kraska, T., Matveeva, M., Moreno, J., Muller, O., Panigada, C., Píkl, M., Pinto, F., Prey, L., Pude, R., Rossini, M., Schickling, A., Schurr, U., Schüttemeyer, D., Verrelst, J., Zemek, F., 2015. Sun-induced fluorescence - a new probe of photosynthesis: First maps from the imaging spectrometer HyPlant. *Glob. Change Biol.* 21, 4673–4684. <https://doi.org/10.1111/gcb.13017>
- Richards, J.A., 1999. *Remote Sensing Digital Image Analysis*.
- Romero, J.M., Cordon, G.B., Lagorio, M.G., 2020. Re-absorption and scattering of chlorophyll fluorescence in canopies: A revised approach. *Remote Sens. Environ.* 246, 111860. <https://doi.org/10.1016/j.rse.2020.111860>
- Romero, J.M., Cordon, G.B., Lagorio, M.G., 2018. Modeling re-absorption of fluorescence from the leaf to the canopy level. *Remote Sens. Environ.* 204, 138–146. <https://doi.org/10.1016/j.rse.2017.10.035>
- Rouse, J.W., Jr., Haas, R.H., Schell, J.A., Deering, D.W., 1974. Monitoring Vegetation Systems in the Great Plains with ERTS. *NASA Spec. Publ.* 351, 309.
- Siegmann, B., Alonso, L., Celesti, M., Cogliati, S., Colombo, R., Damm, A., Douglas, S., Guanter, L., Hanuš, J., Kataja, K., Kraska, T., Matveeva, M., Moreno, J., Muller, O., Píkl, M., Pinto, F., Quirós Vargas, J., Rademske, P., Rodriguez-Moreno, F., Sabater, N., Schickling, A., Schüttemeyer, D., Zemek, F., Rascher, U., 2019. The High-Performance Airborne Imaging Spectrometer HyPlant—From Raw Images to Top-of-Canopy Reflectance and Fluorescence Products: Introduction of an Automatized Processing Chain. *Remote Sens.* 11, 2760. <https://doi.org/10.3390/rs11232760>
- Stoy, P.C., El-Madany, T.S., Fisher, J.B., Gentine, P., Gerken, T., Good, S.P., Klosterhalfen, A., Liu, S., Miralles, D.G., Perez-Priego, O., Rigden, A.J., Skaggs, T.H., Wohlfahrt, G., Anderson, R.G., Coenders-Gerrits, A.M.J., Jung, M., Maes, W.H., Mammarella, I., Mauder, M., Migliavacca, M., Nelson, J.A., Poyatos, R., Reichstein, M., Scott, R.L., Wolf, S., 2019. Reviews and syntheses: Turning the challenges of partitioning ecosystem evaporation and transpiration into opportunities. *Biogeosciences* 16, 3747–3775. <https://doi.org/10.5194/bg-16-3747-2019>
- Sun, Y., Frankenberg, C., Jung, M., Joiner, J., Guanter, L., Köhler, P., Magney, T., 2018. Overview of Solar-Induced chlorophyll Fluorescence (SIF) from the Orbiting Carbon Observatory-2: Retrieval, cross-mission comparison, and global monitoring for GPP. *Remote Sens. Environ.* 209, 808–823.
- Sun, Y., Frankenberg, C., Wood, J.D., Schimel, D.S., Jung, M., Guanter, L., Drewry, D.T., Verma, M., Porcar-Castell, A., Griffis, T.J., Gu, L., Magney, T.S., Köhler, P., Evans, B., Yuen, K., 2017. OCO-2 advances photosynthesis observation from space via solar-induced chlorophyll fluorescence. *Science* 358. <https://doi.org/10.1126/science.aam5747>
- Tagliabue, G., Panigada, C., Dechant, B., Baret, F., Cogliati, S., Colombo, R., Migliavacca, M., Rademske, P., Schickling, A., Schüttemeyer, D., Verrelst, J., Rascher, U., Ryu, Y.,

- Rossini, M., 2019. Exploring the spatial relationship between airborne-derived red and far-red sun-induced fluorescence and process-based GPP estimates in a forest ecosystem. *Remote Sens. Environ.* 231, 111272. <https://doi.org/10.1016/j.rse.2019.111272>
- Thompson, R.L., Goel, N.S., 1998. Two models for rapidly calculating bidirectional reflectance of complex vegetation scenes: Photon spread (PS) model and statistical photon spread (SPS) model. *Remote Sens. Rev.* 16, 157–207. <https://doi.org/10.1080/02757259809532351>
- Tou, J.T., Tou, T.-C., Gonzalez, R.C., 1974. *Pattern Recognition Principles*. Addison-Wesley Publishing Company.
- Verrelst, J., Malenovsky, Z., van der Tol, C., Camps-Valls, G., Gastellu-Etchegorry, J.-P., Lewis, P., North, P., Moreno, J., 2018. Quantifying Vegetation Biophysical Variables from Imaging Spectroscopy Data: A Review on Retrieval Methods. *Surv. Geophys.* 1–41. <https://doi.org/10.1007/s10712-018-9478-y>
- Verrelst, J., Rivera, J.P., van der Tol, C., Magnani, F., Mohammed, G., Moreno, J., 2015. Global sensitivity analysis of the SCOPE model: What drives simulated canopy-leaving sun-induced fluorescence? *Remote Sens. Environ.* 166, 8–21. <https://doi.org/10.1016/j.rse.2015.06.002>
- Vilfan, N., van der Tol, C., Muller, O., Rascher, U., Verhoef, W., 2016. Fluspect-B: A model for leaf fluorescence, reflectance and transmittance spectra. <https://doi.org/10.1016/j.rse.2016.09.017>
- Vilfan, N., van der Tol, C., Yang, P., Wyber, R., Malenovsky, Z., Robinson, S.A., Verhoef, W., 2018. Extending Fluspect to simulate xanthophyll driven leaf reflectance dynamics. *Remote Sens. Environ.* 211, 345–356. <https://doi.org/10.1016/j.rse.2018.04.012>
- Wagner, F.H., Ferreira, M.P., Sanchez, A., Hirye, M.C.M., Zortea, M., Gloor, E., Phillips, O.L., de Souza Filho, C.R., Shimabukuro, Y.E., Aragão, L.E.O.C., 2018. Individual tree crown delineation in a highly diverse tropical forest using very high resolution satellite images. *ISPRS J. Photogramm. Remote Sens., SI: Latin America Issue 145*, 362–377. <https://doi.org/10.1016/j.isprsjprs.2018.09.013>
- Widlowski, J.-L., Lavergne, T., Pinty, B., Verstraete, M., Gobron, N., 2006. Rayspread: A Virtual Laboratory for Rapid BRF Simulations Over 3-D Plant Canopies, in: Graziani, F. (Ed.), *Computational Methods in Transport, Lecture Notes in Computational Science and Engineering*. Springer Berlin Heidelberg, pp. 211–231.
- Widlowski, J.-L., Pinty, B., Lopatka, M., Atzberger, C., Buzica, D., Chelle, M., Disney, M., Gastellu- Etchegorry, J.-P., Gerboles, M., Gobron, N., Grau, E., Huang, H., Kallel, A., Kobayashi, H., Lewis, P.E., Qin, W., Schlerf, M., Stuckens, J., Xie, D., 2013. The fourth radiation transfer model intercomparison (RAMI-IV): Proficiency testing of canopy reflectance models with ISO-13528. *J. Geophys. Res. Atmospheres* 118, 6869–6890. <https://doi.org/10.1002/jgrd.50497>
- Widlowski, J.-L., Robustelli, M., Disney, M., Gastellu-Etchegorry, J.-P., Lavergne, T., Lewis, P., North, P.R.J., Pinty, B., Thompson, R., Verstraete, M.M., 2008. The RAMI On-line Model Checker (ROMC): A web-based benchmarking facility for canopy reflectance models. *Remote Sens. Environ.* 112, 1144–1150. <https://doi.org/10.1016/j.rse.2007.07.016>
- Widlowski, J.-L., Taberner, M., Pinty, B., Bruniquel- Pinel, V., Disney, M., Fernandes, R., Gastellu- Etchegorry, J.-P., Gobron, N., Kuusk, A., Lavergne, T., Leblanc, S., Lewis, P.E., Martin, E., Möttus, M., North, P.R.J., Qin, W., Robustelli, M., Rochdi, N., Ruiloba, R., Soler, C., Thompson, R., Verhoef, W., Verstraete, M.M., Xie, D., 2007. Third

- Radiation Transfer Model Intercomparison (RAMI) exercise: Documenting progress in canopy reflectance models. *J. Geophys. Res. Atmospheres* 112. <https://doi.org/10.1029/2006JD007821>
- Wu, H., Li, Z.-L., 2009. Scale Issues in Remote Sensing: A Review on Analysis, Processing and Modeling. *Sensors* 9, 1768–1793. <https://doi.org/10.3390/s90301768>
- Yang, P., van der Tol, C., 2018. Linking canopy scattering of far-red sun-induced chlorophyll fluorescence with reflectance. *Remote Sens. Environ.* 209, 456–467. <https://doi.org/10.1016/j.rse.2018.02.029>
- Yu, W., Li, J., Liu, Q., Zeng, Y., Zhao, J., Xu, B., Yin, G., 2018. Global Land Cover Heterogeneity Characteristics at Moderate Resolution for Mixed Pixel Modeling and Inversion. *Remote Sens.* 10, 856. <https://doi.org/10.3390/rs10060856>
- Zarco-Tejada, P.J., Berjón, A., López-Lozano, R., Miller, J.R., Martín, P., Cachorro, V., González, M.R., de Frutos, A., 2005. Assessing vineyard condition with hyperspectral indices: Leaf and canopy reflectance simulation in a row-structured discontinuous canopy. *Remote Sens. Environ.* 99, 271–287. <https://doi.org/10.1016/j.rse.2005.09.002>
- Zarco-Tejada, P.J., Camino, C., Beck, P.S.A., Calderon, R., Hornero, A., Hernández-Clemente, R., Kattenborn, T., Montes-Borrego, M., Susca, L., Morelli, M., Gonzalez-Dugo, V., North, P.R.J., Landa, B.B., Boscia, D., Saponari, M., Navas-Cortes, J.A., 2018. Previsual symptoms of *Xylella fastidiosa* infection revealed in spectral plant-trait alterations. *Nat. Plants*. <https://doi.org/10.1038/s41477-018-0189-7>
- Zarco-Tejada, P.J., Hornero, A., Beck, P.S.A., Kattenborn, T., Kempeneers, P., Hernández-Clemente, R., 2019. Chlorophyll content estimation in an open-canopy conifer forest with Sentinel-2A and hyperspectral imagery in the context of forest decline. *Remote Sens. Environ.* 223, 320–335. <https://doi.org/10.1016/j.rse.2019.01.031>
- Zarco-Tejada, P.J., Hornero, A., Beck, P.S.A., Kattenborn, T., Kempeneers, P., Hernández-Clemente, R., submitted. Chlorophyll content estimation in an open-canopy conifer forest with Sentinel-2A and hyperspectral imagery in the context of forest decline. *Remote Sens. Environ.*
- Zarco-Tejada, P.J., Suárez, L., González-Dugo, V., 2013. Spatial Resolution Effects on Chlorophyll Fluorescence Retrieval in a Heterogeneous Canopy Using Hyperspectral Imagery and Radiative Transfer Simulation. *IEEE Geosci. Remote Sens. Lett.* 10, 937–941. <https://doi.org/10.1109/LGRS.2013.2252877>
- Zeng, Y., Badgley, G., Chen, M., Li, J., Anderegg, L.D.L., Kornfeld, A., Liu, Q., Xu, B., Yang, B., Yan, K., Berry, J.A., 2020. A radiative transfer model for solar induced fluorescence using spectral invariants theory. *Remote Sens. Environ.* 240, 111678. <https://doi.org/10.1016/j.rse.2020.111678>
- Zeng, Y., Badgley, G., Dechant, B., Ryu, Y., Chen, M., Berry, J.A., 2019. A practical approach for estimating the escape ratio of near-infrared solar-induced chlorophyll fluorescence. *Remote Sens. Environ.* 232, 111209. <https://doi.org/10.1016/j.rse.2019.05.028>
- Zhao, F., Dai, X., Verhoef, W., Guo, Y., van der Tol, C., Li, Y., Huang, Y., 2016. FluorWPS: A Monte Carlo ray-tracing model to compute sun-induced chlorophyll fluorescence of three-dimensional canopy. *Remote Sens. Environ.* 187, 385–399. <https://doi.org/10.1016/j.rse.2016.10.036>

1152 **List of figure captions**

1153 Figure 1. Location of the study site selected for the quantification of SIF through high-resolution
1154 hyperspectral imaging (left). The red shaded area represents the image coverage. The grey dots
1155 represent the 25×25 m plots that were sampled to obtain the biochemical and structural variables
1156 of the understory, and the white dotted circles represent the radiometric towers with FloX
1157 instruments attached measuring up- and down-welling radiance. The images on the right show
1158 the heterogeneity of the landscape and the understory within the area of study.

1159 Figure 2. Airborne high-resolution hyperspectral flight with the HyPlant sensors (colour-infrared,
1160 {860, 650, 550 nm}) over the study area (a). Yellow squares indicate the location of the $300, 25$
1161 $\times 25$ m, scene grid selection. The different components that comprise a scene can be visually
1162 discriminated by the images acquired from b) the FLUO (false colour, {700, 754, 674 nm}) and
1163 c) DUAL (colour-infrared) sensors of the HyPlant tandem and d) from the digital surface model
1164 of the LiDAR sensor. Spectral radiance extracted from tree crowns, understory (shrubs and
1165 grasses) and soil components of Hyplant DUAL+FLUO images is shown in (e).

1166 Figure 3. Example of a) tree-crown delineation over the b) normalised digital surface model
1167 (nDSM) and the c) True colour DUAL orthoimage.

1168 Figure 4. Understory variability in different scenarios (colour-infrared composition; 25×25 m
1169 pixels along with the collected data) and how this variation affects the mean value in the NDVI
1170 (unitless) and 3FLD ($\text{mW m}^{-2} \text{sr}^{-1} \text{nm}^{-1}$) indices.

1171 Figure 5. Spatial scales from 1 to 100 m (a) and its selection (b) at 5 m (green), 15 m (purple), 25
1172 m (orange), 50 m (yellow) and 100 m (blue). Aggregated values of c) NDVI and d) 3FLD (mW
1173 $\text{m}^{-2} \text{sr}^{-1} \text{nm}^{-1}$) at different spatial scales from a); horizontal lines show the mean tree-crown value
1174 and the Q1-Q3 interquartile range.

1175 Figure 6. Example tree-canopy simulations a) without and b) with understory, c) including their
1176 spectra; d) graphical representation of FLIGHT8.

1177 Figure 7. Model simulation approach diagram.

1178 Figure 8. Relationship between airborne image data obtained from pure tree crowns and
1179 aggregated pixels from a 5 m window to a 100 m window for a) NDVI and b) 3FLD ($\text{mW m}^{-2} \text{sr}^{-1}$
1180 nm^{-1}). Spatial scales start at 5 m (green points) and increase to 15, 25, 50 and 100 m (purple,
1181 orange, yellow and blue points, respectively). Relationship between c) NDVI and d) 3FLD values
1182 aggregated by tree-crown and understory components, and the total aggregated value at 25 m.

1183 Figure 9. Effects of the variation in fluorescence quantum efficiency (F_i , 0 – 0.05) of the forest
1184 understory and the tree crown on the 3FLD ($\text{mW m}^{-2} \text{sr}^{-1} \text{nm}^{-1}$) quantified from 25 m aggregated
1185 pixels against the a) understory LAI and b) 3FLD from tree-crowns. Either only the sunlit
1186 component (left side) or the entire crown (right side) were aggregated. c) Effects of the variation
1187 in LAI (0 – 3) of the forest understory on the relationship between 3FLD calculated from tree-

1188 crowns and 25 m aggregated pixels and d) the associated R^2 and NRMSE values for the linear
 1189 model established for each subgroup of understory LAI.

1190 Figure 10. Relationship between hyperspectral data from 25 m aggregated pixels and model-
 1191 simulated NDVI and 3FLD ($\text{mW m}^{-2} \text{sr}^{-1} \text{nm}^{-1}$) indices accounting for the contribution of SIF of
 1192 the understory (full mode, *a* and *b*, green points with orange dashed line as 1:1 relationship). The
 1193 same relationships obtained from model simulations without accounting for the contribution of
 1194 SIF on the understory and using the empirical reflectance of the background as soil layer (single
 1195 mode, *c* and *d*, light-blue points with a green dashed line as the identity line).

1196 Figure S1. Comparison between different sources of solar irradiance information.

1197 Figure S2. Example of the contribution of scene components for a 25 m window based on the
 1198 relationship between canopy and understory fractional cover (FC) and soil FC shown as different
 1199 intensity orange points.

1200 Figure S3. Comparison of FLIGHT8 with other RTMs using the set of scenarios proposed by the
 1201 RAMI intercomparison exercise. The results of RAMIREF are shown by the dashed light-green
 1202 line and those from other models within the shaded area.

1203 Figure S4. Global bi-directional reflectance factor 1-to-1 comparison (top) and histogram
 1204 differences (bottom) for principal (left) and orthogonal planes (right) within the ROMC-generated
 1205 results.